

Towards High-Precision Exoplanet Photometry with the Huntsman Telescope

By

Jaime Andrés Alvarado Montes

A thesis submitted to Macquarie University
for the degree of Master of Research
Department of Physics and Astronomy
June 2019



MACQUARIE
University
SYDNEY · AUSTRALIA

© Jaime Andrés Alvarado Montes, June 2019.

Typeset in L^AT_EX 2_ε.

This thesis is an account of research undertaken between July 2018 and April 2019 at The Department of Physics and Astronomy, Faculty of Science and Engineering, Macquarie University, Sydney NSW, Australia. Except where acknowledged in a customary manner, the material presented in this thesis is, to the best of my knowledge, original and has not been submitted in whole or part for a degree in any university.



Jaime Andrés Alvarado Montes

Acknowledgements

In pursuing a personal project there are always many people helping you. My main motivation and what keeps me up every day is my family. They are my main interior force and helping them to succeed is essential to me. Thanks for allowing me being away to try to find new horizons in this huge world. I love you, Mom, Dad and my little sister, please accept this piece of my work as a gift.

I want to thank my girlfriend, who is my counsellor, right-hand woman, collaborator, and source of continuous support. Love you! Let's keep up the good work poshoshona, great things are awaiting.

Giant thanks to my supervisors Christian Schwab and Lee Spitler, for sharing all their experience with me and being always attentive to my work. I have learned a lot of them individually while also benefiting greatly from their combined supervision. I will demonstrate that all their efforts are worth every day. Thanks also to Dr. Anthony Horton for all his kindness and endless knowledge, to Wilfred Gee because seeing his work and amazing performance with computers has motivated me to work harder every day, and to all my peers who made a perfect environment to work and enjoy my whole process. Special thanks to Bronwyn Reichardt and James Tocknell, for their valuable comments and suggestions.

Abstract

The Huntsman Telescope, situated at Siding Spring Observatory in Australia, is a cost-effective astronomical imaging system that makes use of an assembly of commercial off-the-shelf optics and detectors. In this thesis, I develop an appropriate set up of Huntsman for the future detection and subsequent follow-up observation of exoplanets around nearby stars, via the transit technique. I also investigate the optimal observational method to reach high-precision photometry when using an array of small lenses which point at the same target; discuss advantages and shortcomings; and ultimately demonstrate the achievable on-sky photometric precision of Huntsman. This includes comparing the precision achieved by combining data from multiple cameras, and for different focusing of the lenses. A key component of this thesis was the development of a photometry pipeline for processing Huntsman data and extracting light curves. Over the next few years, the Huntsman Telescope will become one of the facilities in the Southern Hemisphere using transit photometry to both discover exoplanets, and follow up on exoplanet candidates from ongoing space-based missions.

Contents

Acknowledgements	iv
Abstract	v
Contents	vi
List of Figures	viii
List of Tables	ix
List of Publications	x
1 Introduction	1
1.1 Motivation: Extrasolar Planets	1
1.1.1 Too Many Follow-up Targets, not Enough Telescopes	3
1.1.2 Exoplanets Around Bright stars: TESS	5
1.2 Complications of Ground-Based Observation	7
1.3 Detection Method: Transit Photometry	10
1.4 Thesis Outline	11
2 The Huntsman Telescope	12
2.1 Collection of Multiple Apertures	12
2.1.1 The Huntsman Telescope	12
2.1.2 The Advantages of Huntsman	14
3 Methodology	19
3.1 The Huntsman Telescope in Operation	19
3.1.1 Collection of Data	20
3.2 Characterising Huntsman CCDs	23
3.3 Data Reduction	26
3.3.1 CCD Noise and Bias Subtraction	26
3.3.2 Flat-Fielding Correction	27
3.3.3 Bad Pixels Correction	28

4	Photometry Results	29
4.1	Aperture Photometry	29
4.2	Differential Photometry	30
4.3	Signal-to-Noise and Aperture Radius	33
4.3.1	Selection of Optimal Aperture	35
4.4	HUntsman PHOtometry Pipeline (HUPHOP)	38
4.5	Huntsman Light Curves	40
5	Summary and Discussion	47
5.1	Future Work	50
	Appendix	51
	References	55

List of Figures

1.1	Histogram of confirmed exoplanets using different methods	3
1.2	TESS observation sectors	5
1.3	TESS simulated exoplanet yield	6
1.4	Scintillation noise as a function of exposure time	8
1.5	Ratio of photon and scintillation noise for Huntsman	9
2.1	The dome of Huntsman at Siding Spring Observatory	13
2.2	The Huntsman Telescope	13
2.3	Field of view per facility for various ground-based projects	14
2.4	Effective aperture area per facility for various ground-based projects	15
3.1	Filters transmission curves	22
3.2	TESS target magnitudes for Huntsman	23
3.3	Signal in the Huntsman CCDs as a function of exposure times	24
3.4	Diagrams used to find the gain of the Huntsman CCDs.	25
3.5	Huntsman data reduction process	27
4.1	Differential photometry of HD 224822	31
4.2	Optimal aperture size of a Huntsman defocused camera	36
4.3	Aperture illustration of a Huntsman defocused camera	37
4.4	Optimal aperture size of a Huntsman in-focus camera	38
4.5	Aperture illustration of a Huntsman in-focus camera	39
4.6	Individual light curves with Huntsman in-focus cameras	42
4.7	Integrated light curve from three Huntsman in-focus cameras	43
4.8	Light curve with a Huntsman defocused camera	44
4.9	Evolution of noise sources in HD 224822	45
4.10	Ideal exposure time for telescope defocusing with Huntsman	46
5.1	Photometry precision in four Huntsman cameras	48
5.2	Confirmed TESS planets and Huntsman photometric precision	49
A.1	Differential photometry of Wasp 20: Unexceptional Telescope Tracking	52
A.2	Differential photometry of Hip 65: Unexceptional Telescope Tracking	53
A.3	Differential photometry of TYC 8540-01203-1: Unexceptional Telescope Tracking	54

List of Tables

2.1	SuperWASP-South and the Huntsman Telescope	17
3.1	Report of observational runs made with Huntsman	21
3.2	Gain of the four active Huntsman SBIG STF-8300M cameras	26

List of Publications

- **Jaime A. Alvarado-Montes** and Carolina García Carmona, *Orbital decay of short-period gas giants under evolving tides*. Published in the Monthly Notices of the Royal Astronomical Society¹, Volume 486, Issue 3, Pages 3963-3974, July 2019.
- Mario Sucerquia, **Jaime A. Alvarado-Montes**, Jorge I. Zuluaga, Nicolás Cuello and Christian Giuppone, *Ploonets: formation, evolution and detectability of detached exomoons*. (Resubmitted to MNRAS after first referee report on 1 April 2019.)

¹DOI: <https://doi.org/10.1093/mnras/stz1081>

What other conclusion shall we draw from this difference, Galileo, than that the fixed stars generate their light from within, whereas the planets, being opaque, are illuminated from without; that is, to use Bruno's terms, the former are suns, the latter, moons, or earths?

Johannes Kepler, *Dissertatio cum Nuncio Sidereo*^a, 1610

^aAs translated by E. Rosen in *The Sources of Science*", No. 5, 1965, in *Kepler's Conversation with Galileo's Sidereal Messenger*"

1

Introduction

1.1 Motivation: Extrasolar Planets

The existence of planets beyond our Solar System has been speculated for a long time. The philosopher Epicurus wrote in the fourth century BC: “*there are infinite worlds both like and unlike this world of ours*”, and thinkers such as Giordano Bruno and Christiaan Huygens adopted this idea during the Renaissance and Enlightenment in Europe. The first claim of an exoplanet detection was made by [Jacob \(1855\)](#) who thought he had measured perturbations of a sub-stellar companion on the binary system 70 Ophiuci¹. Modern techniques to detect exoplanets, however, are often traced to a short paper by [Struve \(1952\)](#), where both the measurement of variations in the star's relative speed (radial velocity) and the drop in stellar flux (transits) were proposed.

About 70 years after Struve's paper, the research in exoplanetary science has brought thousands of confirmed extrasolar planets (see [Figure 1.1](#) using the database from [Schneider, J. et al. 2011](#)), as well as hundreds of candidates whose planetary nature is unconfirmed and awaits a detailed follow-up. Among these discoveries it is worth mentioning some phenomena with a shortage of clear explanation. For instance, the discovery of the first sub-stellar companion by [Mayor & Queloz \(1995\)](#) led to the concept of *hot Jupiters*, with large masses ($M_p \sim 0.1 - 13.6 M_{\text{Jup}}$) and very short orbital periods ($P < 10$ days) ([Takeda & Rasio 2005](#), [Lithwick & Naoz 2011](#) and see [Dawson & Johnson 2018](#) for a recent and complete review). This was contrary to what was expected from the theories for the formation and evolution of giant planets in that time (see [Lissauer 1987](#) and references therein), which should form in distant orbits to accrete all of their gas component ([Ikoma et al., 2000](#), [Udry & Santos, 2007](#)), and then migrate to closer distances from the star ([Morbideilli et al., 2009](#)).

¹Which later turned out to be a multiplanet system composed of planets with masses between 0.46 and 12.8 Jovian masses, which orbit the binary system in distances from 0.05 to 5.2 AU ([Wittenmyer et al., 2006](#))

Different strategies for doing high precision photometry of stars, aimed at following up on exoplanets, have been explored before ([Henry et al., 1997](#), [Baliunas et al., 1997](#), [Henry, 1999](#)). The discovery of transiting exoplanets in the late 90's allowed us to achieve new physical information for both the star and the planet ([Charbonneau et al., 2000](#), [Henry et al., 2000](#)), and the discovery of many 51 Pegasi-like planets ([Mayor & Queloz, 1995](#)) has motivated further studies for detecting exoplanets.

The follow-up of exoplanets led to the discovery of the first organic molecule in an extrasolar atmosphere – methane in HD 189733b ([Swain et al., 2008](#)). One of the most important results came in 2013 when Mikko Tuomy from University of Hertfordshire, UK, indicated for the first time the possibility of an Earth-sized planet around Proxima Centauri. This was later confirmed in 2016 by [Anglada-Escudé et al. \(2016\)](#) through an initiative of the European Southern Observatory, the *Pale Red Dot* campaign, using a 3.6-m telescope in La Silla, Chile, as well as other facilities. The planet became known as Proxima b: the closest planet to the Solar System. As the field of exoplanet astronomy becomes established, other unexpected observational results are providing new constraints on theoretical aspects of planet formation. For example: the unusual spectroscopic signatures of the stars HD 240430 and HD 240429 (named Kronos & Krios by [Oh et al. 2018](#)) showing deep trails of heavy elements that suggest recent planetary merging, the new-found puzzling light curves of KIC-8462852 (nicknamed Tabby's star [Boyajian et al. 2016](#)) attributed to a combination yet-to-be-confirmed between a Jupiter-like planet and a Neptune-like exomoon ([Teachey & Kipping, 2018](#)), and the hypothesised exocometary signatures from KIC 12557548 and KIC 3542116 ([Rappaport et al., 2012, 2018](#)).

Exoplanet observations have yielded significant discoveries in the last three decades. However, many of these discoveries still remain unconfirmed, and different teams have tried to corroborate them by using space- and ground-based telescopes all over the world. Interestingly, most newly-discovered systems are quite different to the Solar System, and the diverse variety of exoplanets prompts a number of outstanding questions: Did these planets form in the same way as those in the Solar System? Is it possible to find Earth-like planets around Sun-like stars? Is there a chance that extrasolar life dwells on these exo-worlds? Through the contemporary knowledge of planets achieved mostly from our own Solar System, some of these questions have a partial answer now, whereas others remain completely unanswered and need further work to be solved.

To add to the observational data on exoplanets, I aim at using the Huntsman Telescope over the next few years with the transit photometry technique, and to do that I need to prove that Huntsman is a facility capable of achieving high-quality photometry precision. Once I have investigated the

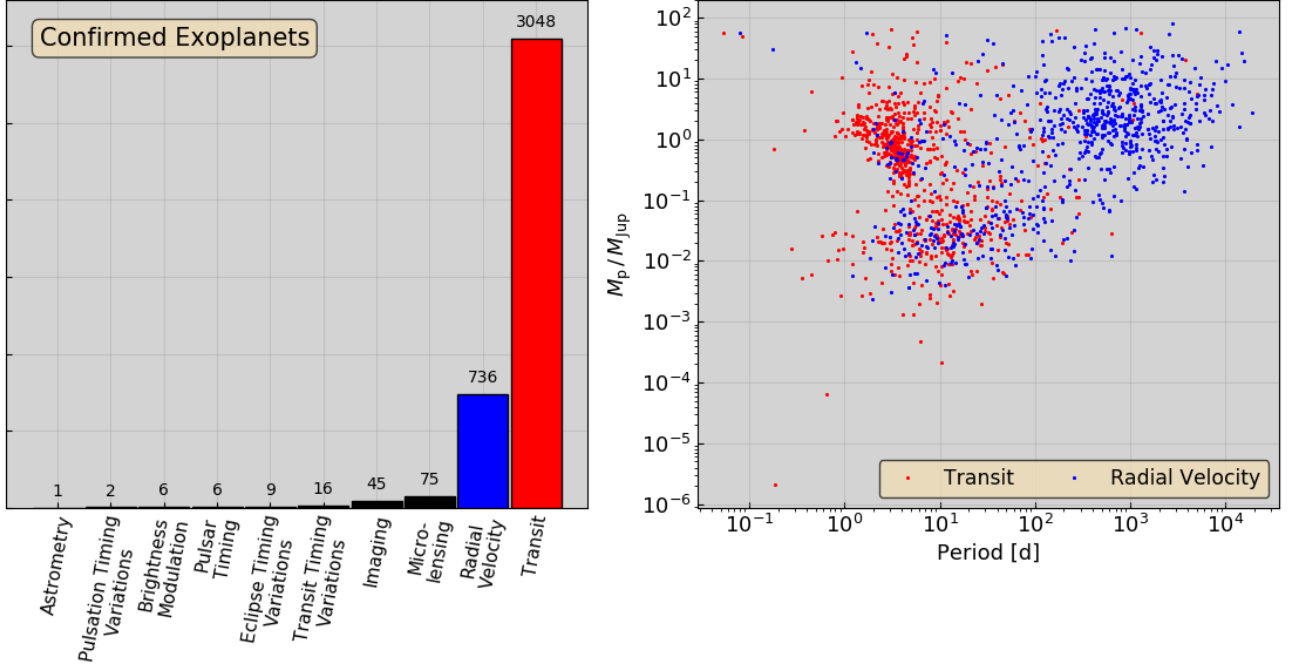


FIGURE 1.1: *Left-hand panel:* Confirmed exoplanets using different methods, where both the Radial Velocity (blue) and Transit (red) techniques show an evident success to find exoplanets. *Right-hand panel:* Planetary mass (M_p) and orbital period (P) distribution for detected planets using RV measurements and transits. Most of the planets are massive ($M_p > 0.1 M_{Jup}$) and lie on close-in orbits ($P < 10$ days). Both methods show a bias towards detecting giant planets, since both the photometric and gravitational effects they produce on their host stars are much stronger than those of smaller planets. This plot uses the exoplanet.eu database of [Schneider, J. et al. \(2011\)](#). The data for this plot was downloaded on the 21st April 2019.

optimal parameters to achieve the best on-sky photometry with Huntsman, which is the main topic of this thesis, my main goal will be to do a continuous follow-up of exoplanet candidates. As many of the stars being studied at this moment by ongoing space-based missions are bright, their detection and investigation with ground-based facilities like Huntsman is more feasible. Thus, the long-term result of this thesis, as well as the research I will perform during my PhD, will be a contribution from exoplanet observations to the current models that account for the formation and evolution of planetary systems, getting a better insight into many of the discovered baffling phenomena not well understood at this time. The follow-up of exoplanet candidates will be a crucial part of this research.

1.1.1 Too Many Follow-up Targets, not Enough Telescopes

The number of unconfirmed exoplanet candidates from space-based missions will vastly surpass the follow-up capabilities on Earth. In fact, with the improvement of planet-hunting facilities and planet-detection techniques, many Jupiter- and Neptune-like exoplanet candidates are being found, as shown in this section. Their confirmation will need monitoring from the ground, and with Huntsman I can

contribute to this extensive work. That said, the main purpose of this thesis is to find out what the achievable precision of an array of lenses like *Huntsman* is, as well as carrying out the appropriate analysis for the combination of data from its multiple cameras.

To date just few exoplanets have been detected by direct imaging, since it is very difficult to resolve them from their host star. If we compare the brightness of a planet to that of a star, we know the former is a very faint light source that fades out due to the intense stellar shine. In real terms, a Sun-like star is thousands of millions times brighter than all of the planets in orbit around it, so astronomers must use indirect methods to detect exoplanets. Several different techniques have shown a remarkable success as depicted in [Figure 1.1²](#) – [Rosenblatt \(1971\)](#) discussed for the first time the detection of an extrasolar system using the transit method, opening a big gate for ceaseless efforts in the hunting of planets.

Since the first transiting exoplanet was discovered by [Charbonneau et al. \(2000\)](#) using a relatively small telescope, 10-cm aperture diameter, numerous ground-based projects have followed this approach, some of them employing networks of small (~ 20 cm) aperture telescopes to observe from 10^4 to 10^5 stars. These projects include, but are not limited to, the Hungarian Automated Telescope Network (HATNet, [Bakos et al. 2002, 2013](#)), the Wide Angle Search for Planets (WASP, [Street et al. 2003](#)), the Kilodegree Extremely Little Telescope (KELT, [Pepper et al. 2007](#)), the MEarth project ([Irwin et al., 2009](#)); and highly productive space-based missions such as: Microvariability and Oscillations of Stars (MOST, [Rucinski et al. 2003](#)), COROT (see [Auvergne et al. 2009](#)), and Kepler ([Borucki et al., 2010](#)).

Kepler has discovered ~ 3000 exoplanets using the transit method ([Burke et al., 2015](#)), but most orbit faint stars and cannot be efficiently followed up from the ground using the current technology. After one of the reaction wheels of *Kepler* failed, the new target stars of *Kepler* (i.e. the new mission *K2*) were brighter. This has allowed a broader range of facilities to contribute by detecting and confirming new exoplanets (e.g. [Vanderburg & Johnson 2014](#), [Crossfield et al. 2015](#), [Vanderburg et al. 2016](#)).

Radial Velocity (RV) surveys have led to more than 700 planets confirmed thus far: the gravitational-induced variations that stars undergo when they are being pulled by an orbiting planet, allow spectrographs such as the High Accuracy Radial velocity Planet Searcher (HARPS; [Mayor et al. 2003](#)) or the Echelle SPectrograph for Rocky Exoplanet- and Stable Spectroscopic Observations (ESPRESSO; [Pepe et al. 2010](#)) to measure the Doppler shifts in the stellar spectra.

²For an updated download and filtering of data visit www.exoplanet.eu

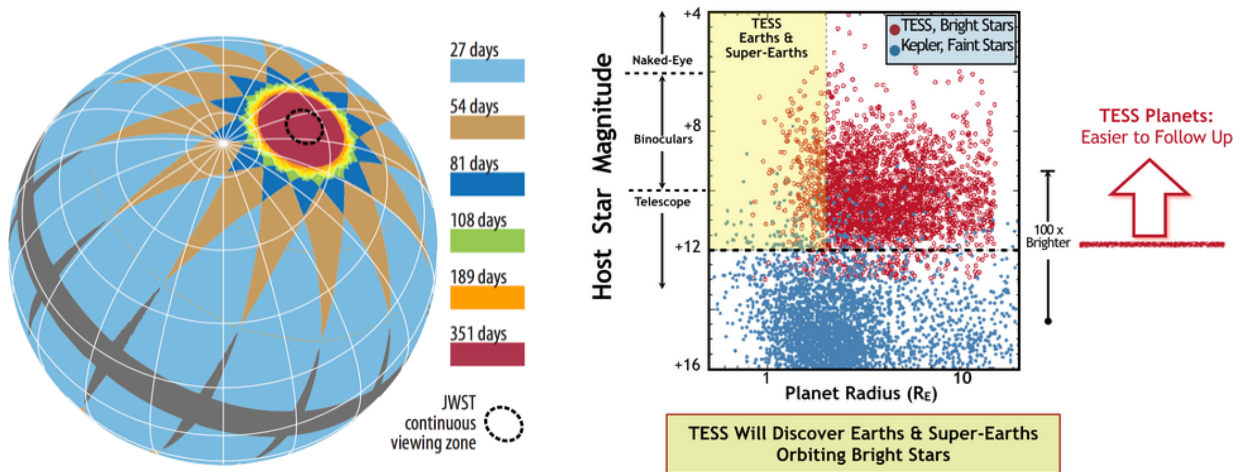


FIGURE 1.2: *Left-hand panel:* Time spent by TESS on each sector, including coverage of overlapping areas. Some of these regions have a continuous monitoring in each hemisphere. *Right-hand panel:* TESS candidate exoplanet host stars, which are significantly brighter than those of the Kepler space mission (most of them are even visible with binoculars), and thus enable their follow-up with both ground- and space-based telescopes. Left-hand image credit: [Ricker et al. \(2015\)](#). Right-hand image credit: Massachusetts Institute of Technology, MIT (<https://heasarc.gsfc.nasa.gov/docs/tess/primary-science.html>).

In the future, the number of exoplanets to follow up will grow significantly with forthcoming ground- and space-based missions like the Large Synoptic Survey Telescope (LSST; [Lund et al. 2015](#), [Jacklin et al. 2015, 2017](#)), the CHAracterising ExOPlanet Satellite (CHEOPS, [Beck et al. 2017](#)), the PLANetary Transits and Oscillations of stars (PLATO; [Rauer et al. 2014](#)), and the low earth orbit visible and infrared exoplanet spectroscopy observatory (TWINKLE; [Savini et al. 2018](#)). These missions will provide thousands of rocky and gas planets to be monitored.

1.1.2 Exoplanets Around Bright stars: TESS

The Transiting Exoplanet Survey Satellite, TESS ([Ricker et al., 2015](#)), which started observing in August 2018, is scanning nearby stars to find Earth- and Neptune-sized planets ([Sullivan et al., 2015](#), [Sullivan et al., 2017](#)). The TESS target stars are $\sim 30 - 100$ times brighter than Kepler and K2 stars, allowing efficient ground-based follow-up. TESS is observing 13 different sectors in both hemispheres, covering almost 85% of the celestial sphere (i.e. an area 400 times larger than the one Kepler monitored), as shown in the left-hand panel of [Figure 1.2](#) ([Ricker et al., 2015](#)). Each sector is observed by TESS over an average time of 27 days before going to the next sector, and there is no option according to the primary mission specifications to revisit the sectors, *so follow-up or searches for longer-period exoplanets must be conducted with other facilities.*

TESS exoplanets will enable the community to do a systematic follow-up. These planets will be

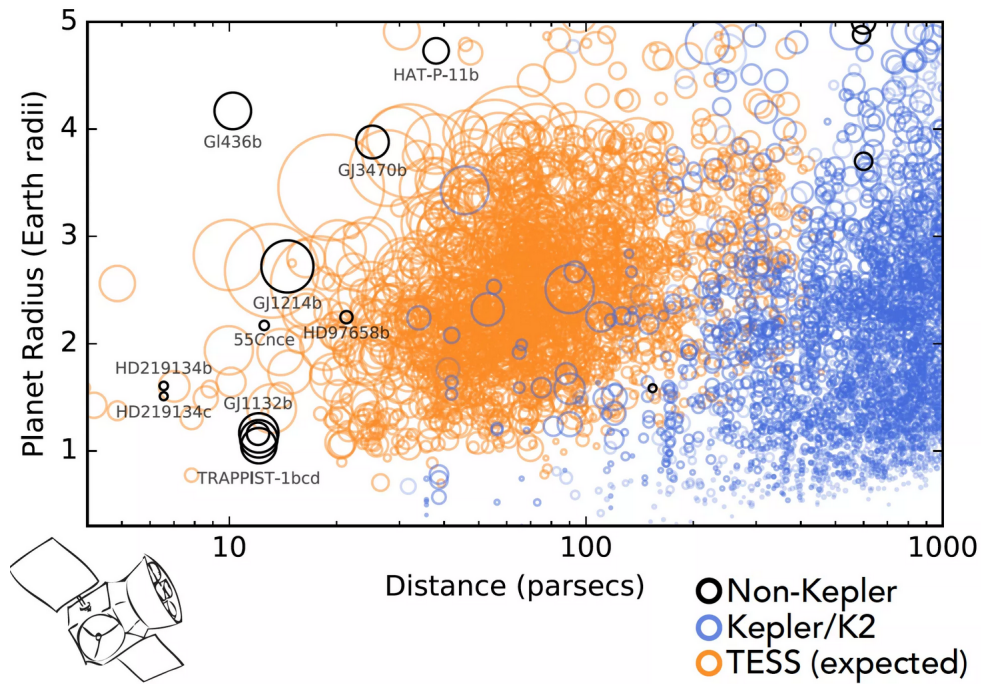


FIGURE 1.3: Simulated yield of TESS exoplanet detections. Image credit: Zach Berta-Thompson

studied to find the optimal targets for further exoplanet atmospheric characterisation using facilities like NASA’s James Web Space Telescope, JWST (Cowan et al., 2015, Batalha et al., 2017, Benneke et al., 2017). The ultimate data product of TESS will be a catalogue listing most of the brightest main-sequence stars that harbour transiting exoplanets (see the right-hand panel of Figure 1.2). As will be shown, such a large number of bright targets is ideal for a Huntsman-like system. Indeed, for its relatively low-cost it will be an ideal system to duplicate, helping to address the major problem of following up so many exoplanets.

Depending on the ecliptic latitude (and hence the overlap between sectors) TESS is more or less sensitive to certain planetary orbital periods. A region closer to the ecliptic will usually have 27 days of coverage, so most TESS exoplanet candidates will lie in close-in orbits where TESS will have a detection efficiency relatively high. Those transiting exoplanets with longer periods could be monitored in regions which overlap near to the ecliptic poles. The TESS exoplanet yield will be highly significant (see Figure 1.3), where the fraction of 2-transit TESS planets and planet candidates will necessitate additional follow-up. For tracing the planetary orbit of such candidates we will need ideally 3 transits or more, and with Huntsman we can complement these follow-up observations from the ground.

1.2 Complications of Ground-Based Observation

Professional ground-based telescopes typically work from locations where both the weather and topography are optimal, such as Mauna Kea in Hawaii, or the Atacama desert in Chile. However, even these ideal locations have atmospheric blurring, which cause stars, that otherwise would be point sources, to appear as slightly broadened and varying with time. This leads to a reduction in spatial resolution, as well as in the signal-to-noise of observations as described in detail in this section.

As the light passes through the atmosphere, it follows a path crossing different air layers, whose temperature depends on their altitude. As density depends on temperature, this results in an optical path which is across sections of the atmosphere with different refractive indexes, with spatial and temporal variations. This effect is equivalent to a light ray changing from one medium to another, which in physics is known as refraction. *Turbulence* in the upper atmosphere changes the light path constantly, and the result is usually a distorted image, that is highly variable in time, an effect called *seeing*. Furthermore, the turbulent air locally focuses and defocuses the wavefront of a star, which, in addition to blurring, leads to an apparent change in the stellar brightness, an effect known as *scintillation*.

A consequence of scintillation is the twinkling of stars that we all know from observing the night sky. Scintillation limits the achievable precision of photometric observations. It is [Young \(1967\)](#) who describes the scintillation noise during an exposure, σ_{scint} , using an approximation given by,

$$\sigma_{\text{scint}} = 1.5 \sqrt{1 + \frac{1}{n_E}} [10 \times 10^{-6} D^{-\frac{2}{3}} (\cos \gamma)^{-1.75} (t_{\text{exp}})^{-\frac{1}{2}} e^{-\frac{2h}{h_o}}] \quad (1.1)$$

where D is the telescope's diameter in meters, n_E the number of uncorrelated reference stars ([Kornilov, 2012](#)), γ the angle from zenith (airmass), t_{exp} the exposure time in seconds, h the elevation of the place (1164 m for Siding Spring Observatory), and h_o the atmospheric scale altitude ($\simeq 8000$ m). The constant 10×10^{-6} factor has units of $\text{m}^{2/3} \text{s}^{1/2}$, to give σ_{scint} in units of relative flux (see [Dravins et al. 1998](#)). The exponent of the airmass ranges from 1.5 to 2.0, and depends on the wind's direction ([Southworth et al., 2009a](#)). In [Figure 1.4](#) we can see how scintillation varies depending on the exposure time and the effective aperture diameter. In this Figure the black and blue line represent the present and future array of Huntsman lenses, respectively.

Photons are randomly emitted from the surface of the star and are therefore recorded by the detector in a stochastic way. The associated uncertainty of the number of photons that strike an imaging detector on Earth each second, known as *photon noise*, is given by the following expression:

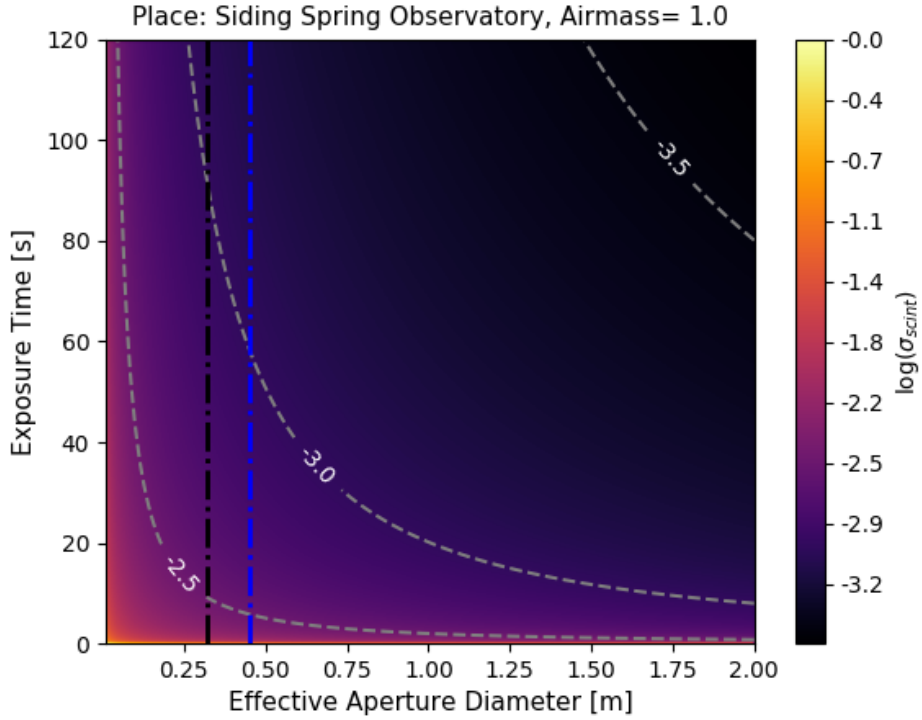


FIGURE 1.4: Scintillation dimensionless amplitude error (σ_{scint}), as a function of exposure time and effective aperture diameter. We assume an airmass equal to 1 for an instrument located at Siding Spring Observatory (altitude 1164 m). As we can notice in this plot, the collection of five lenses $D \sim 0.32$ m (dashed black line) that Huntsman uses at the moment, dwells in a region where scintillation produces an amplitude error $\sim 0.1\%$ of the signal. Assuming bright targets like those from TESS, we could use exposure times ranging from 15 seconds (in-focus photometry) to 100 or more seconds (defocused photometry), and still be outside of the region where scintillation reaches $\sim 0.35\%$. The dashed blue line stands for the final Huntsman 10-lenses design ($D \sim 0.45$ m), so that scintillation is even more negligible for the same range of exposure times.

$$\sigma_{\text{phot}} = \frac{2}{D\sqrt{\pi t_{\text{exp}}\delta\lambda\Phi}}, \quad (1.2)$$

with Φ as the stellar flux, and $\delta\lambda$ the wavelength bandwidth.

In ground-based photometry, scintillation noise (Eq. 1.1) and photon noise (Eq. 1.2), are commonly the most dominant noise sources. Hence, it is useful to consider both as in Figure 1.5, where they are related to the parameter space of stellar magnitudes and telescope size (i.e. the diameter D). We have assumed a telescope throughput of 100%, and a perfect charge-coupled device (CCD) detector with a quantum efficiency (QE) of 1. There are no contributions from dark current or readout noise, as well as no sky background. The upper horizontal solid line corresponds to a region where the scintillation and photon noise contribute the same to the total error – for bright stars where $m_V \lesssim 13$, the observations will be dominated by scintillation independently of the size of the telescope. At the other extreme, faint stars are always limited by the number of photons hitting the detector, which

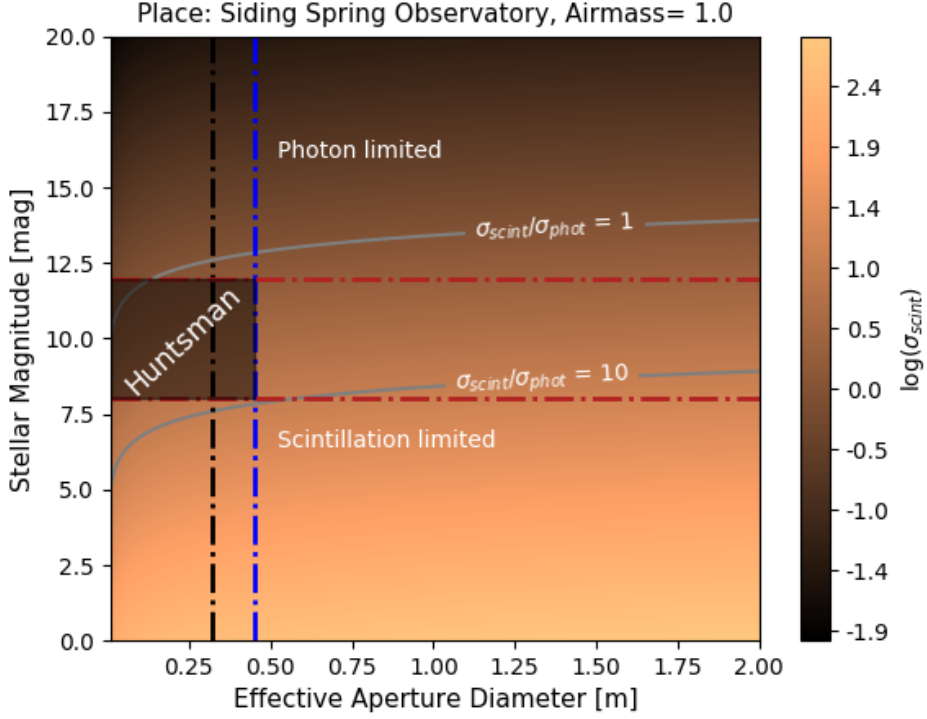


FIGURE 1.5: Comparison between the expected dimensionless amplitudes of photon noise (σ_{phot}) and scintillation (σ_{scint}), for different stellar magnitudes and effective aperture diameters. We assume an airmass equal to 1 for a telescope located at Siding Spring Observatory (altitude 1164 m). The dashed horizontal lines (red) represent stars with magnitudes ranging from 8 to 12 mag (see Figure 1.2 and Figure 3.2) in the Johnson System, which is typical for most of the TESS host exoplanet stars. The dashed vertical lines represent the effective aperture diameter of the Huntsman Telescope at the present design of five lenses (black), and the final 10-lenses design (blue) – 0.32 and 0.45 m, respectively. We can see that Huntsman lies in a regime where both photon and scintillation noise are roughly comparable, while the latter dominates for typical TESS targets.

makes sense because any variation in the number of released photons from the star would be more significant in fainter stars. Moreover, the sky background subtraction is also important because the noise in the background is proportionally higher for faint stars.

The spatial intensity of scintillation variations in the pupil plane of a telescope, or *speckles*, are caused by turbulence in the upper atmosphere (Osborn et al., 2015). Their characteristic size is determined by the radius of the first Fresnel zone, $r_F = \sqrt{z\lambda}$, which is the area between the turbulent layer and the CCD where the interference of waves is constructive. Here z is the distance of propagation from the turbulent layer to the telescope, and λ is the wavelength of light. These speckles often reach the order of several centimetres; for example, if the turbulent layer is located at 7 km and observed at 580 nm, the ensuing speckles are ~ 0.06 m, independent to the turbulence’s strength.

Water vapour, which is mostly concentrated in the lower part of the atmosphere, forms clouds of different sizes that can affect exoplanet observation, as they change on shorter time-scales than an

exoplanet transient event. In observational astronomy, these transparency variations can be avoided by choosing a good site at a high altitude and with good weather, and observing during what is often called a night of optimal photometric conditions (see [Mann et al. 2011](#)). Differential photometry plays an important role in mitigating transparency variations, as will be shown in Chapter 4.

The Earth’s atmosphere contains chemical elements which absorb light at different wavelengths of the spectrum, with the primary molecular absorption lines being due to water, ozone, and oxygen (known as telluric absorption). Another issue for ground-based observations is the preferential scattering of bluer light due to small particles in the atmosphere. To reduce the effect of atmospheric absorption, we can use filters that isolate the observation to less affected sections of the object’s spectrum. The most commonly used broad-band filters work on wide bandpass (e.g. $u' g' r' i' z'$ of the SDSS [Fukugita et al. 1996](#), and Johnson-Cousins UBVRI [Bessell 1990](#)), which are all affected by a considerable number of absorption lines.

As will be discussed in [section 4.2](#), differential photometry essentially calibrates the incoming flux of the target star using some nearby reference stars. These stars will always have subtle differences in the total airmass (i.e. the column of air above the telescope towards the star’s location). Such differences can give rise to another noise source known as first-order differential extinction, whose amplitude is very small and highly-dependent on the observing conditions ([Mann et al., 2011](#)). Furthermore, this type of extinction also varies for stars of different spectral type, producing a colour effect that is known as second-order differential extinction. Therefore, to work with differential photometry we must do a careful selection of the reference stars, so it is preferable to have both the target and the reference stars emitting light in the same part of the spectrum, or at least in close spectral types.

1.3 Detection Method: Transit Photometry

During a “planetary transit” a dip is produced in the stellar flux when an exoplanet crosses in front of its parent star. It can be measured with flux time series (called light curves), which show the planetary orbit – see review of this method in [Borucki & Summers \(1984\)](#). The fractional stellar flux drop during transit for a star of radius R_\star , and a planet with radius R_p has a depth of:

$$\delta f = \left(\frac{R_p}{R_\star} \right)^2 \quad (1.3)$$

assuming that only the host star contributes to the luminosity, and that the whole disk of the planet is eclipsed ([Seager 2010](#)).

The orbital path of a planet does not always cross the surface of its parent star, in which case we can never see a transit event. Systems with an inclined orbit with respect to the line of sight from Earth cannot be observed with the transit technique. Even when the inclination is low enough for a transit to take place, a star has an enormous size compared to that of a planet, so in consequence the stellar flux drops just a tiny fraction of $\sim 0.01 - 2\%$ (Gilliland et al. 1993, Johnson et al. 2009, Croll et al. 2011, Colón et al. 2012, Tregloan-Reed & Southworth 2013, Zhao et al. 2014, Fukui et al. 2016, Stefansson et al. 2017), which in principle could be unnoticed if it is too subtle. This is a great obstacle for the transit technique, because the probability that such an alignment occurs is very small, given by

$$\text{probability} = \left(\frac{R_{\star} + R_p}{a_p} \right) \left(\frac{1 + e \sin \omega}{1 - e^2} \right), \quad (1.4)$$

where e is the planet's orbital eccentricity, ω is the argument of the periape, and a_p is the semimajor axis of the planet (Seager, 2010). A planet in a 1-AU orbit around a Sun-like star has a transit probability of just 0.47%. However, with transit surveys where hundreds of thousands of stars are observed, this method starts to become highly competitive with other methods (Hidas et al., 2005).

An important feature of the transit method is the determination of the size of the planet from the light curve obtained with the transit (see Equation 1.3). When combined with the results of radial velocity measurements, which yield a mass estimate, one can measure a planet's average density and hence make an initial guess at its overall composition.

1.4 Thesis Outline

This thesis develops an observational and methodological plan for the future use of the Huntsman Telescope to observe exoplanets orbiting around bright stars. Chapter 2 includes a description of the Huntsman Telescope, and how it may contribute to the present ground-based follow-up observations of exoplanets. In Chapter 3, I give a general overview of how the Huntsman data for this thesis was collected, as well as the basic steps to calibrate it. Then, I introduce aperture photometry in Chapter 4 as the working technique to analyse Huntsman data. This includes the explanation of the HUNtsman PHOtometry Pipeline (HUPHOP) developed to perform time-series photometry. The main results of the achievable on-sky precision of Huntsman are also given. Finally, in Chapter 5 I discuss the outcomes of this thesis in terms of the present state of Huntsman, and the upcoming work necessary to further optimise the facility in order to become a highly productive system in the observation of exoplanet transit events.

2

The Huntsman Telescope

Small aperture telescopes have been used to make important discoveries in astronomy, and are an important part in the follow-up of exoplanets. The size of a telescope, also called an *aperture*, refers to the diameter (D) of its light-collecting area. While a small collecting area means less light, using several small apertures to observe from different parts of the world is a great way to follow up the large number of exoplanet candidates. The main advantage of small telescopes is that they are relatively cheap and can be deployed without million-dollar investments (Oswalt, 2003). In this section I describe the main characteristics, advantages, and drawbacks of the Huntsman Telescope, an array of small apertures that will be used in the future for follow-up observations of exoplanet candidates.

2.1 Collection of Multiple Apertures

2.1.1 The Huntsman Telescope

The Huntsman Telescope, located in Australia (see Figure 2.1), is an imaging system where multiple lenses (5 currently, 10 planned) are simultaneously pointing at the same target at visible wavelengths. By combining data from each lens, the achievable signal-to-noise scales approximately with the square root of the number of lenses, as they are looking at the same Field of View (FOV) and hence the effective aperture increases (Law et al., 2015). A distinct advantage, that will be discussed further below, is that multiple lenses allow better mitigation of systematic errors, such as pixel-to-pixel and intra-pixel sensitivity variations.

Each of Huntsman's Canon 400mm f/2.8L telephoto lenses, with an aperture diameter $D \approx 0.143$ m, is paired with an individual SBIG STF-8300M CCD camera (see Figure 2.2). The effective aperture of the telescope is $N \times (\pi \times 0.07^2) \text{ m}^2$, where N is the number of lenses. The focal length is that of a



FIGURE 2.1: Huntsman dome at Siding Spring Observatory (SSO), Coonabarabran, NSW, Australia, at an altitude of ~ 1150 m. The seeing is unexceptional, but SSO has extremely dark skies. Huntsman is in a 4.5 m diameter fibreglass dome with a 1.2 m wide aperture, manufactured by Astrodomes of Queensland, Australia. The battery of the dome shutter is charged by a solar panel that can be seen on the dome (upper left). The telescope will run in a fully automated mode, so the dome has its own weather station and internal/external monitoring cameras. The 4-m Anglo-Australian Telescope is behind Huntsman on the right side of the photo. This photo was taken during a visit the author made to SSO in August 2018.



FIGURE 2.2: The Huntsman Telescope is now composed of five Canon 400mm f/2.8L IS II USM telephoto lenses, each with an SBIG STF-8300M CCD. It also has a Celestron 11" f/2.2 Rowe-Ackermann Schmidt Astrograph (RASA) telescope with an FLI ML501000 camera, to be used alongside the five lenses for a thorough comparison of imaging performance. Image courtesy of Anthony Horton.

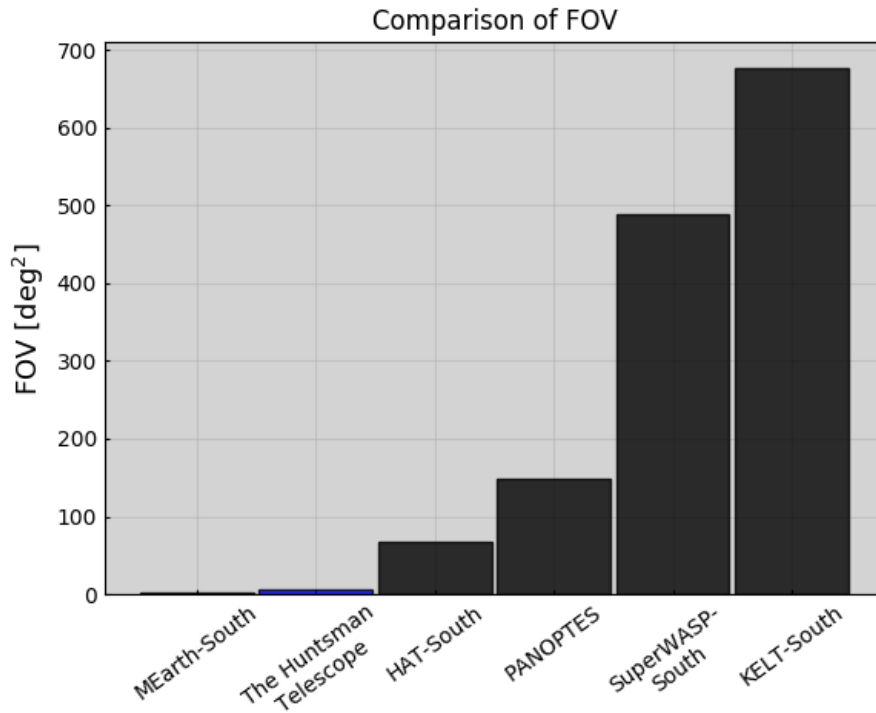


FIGURE 2.3: Field of view per facility for various ground-based projects making observations of exoplanets. PANOPTES values are given by [Gee et al. \(2016\)](#), and the remainder are extracted from [Law et al. \(2015\)](#).

single lens (i.e. 0.4 m), which in turn increases the system’s imaging speed. This setup differs to other exoplanet projects like SuperWASP ([Street et al., 2003](#)), with an aperture diameter $D \approx 0.11$ m (see [Table 2.1](#)), which points each lens at a different field. Although they get a much wider FOV in order to conduct wide-field surveys (see [Figure 2.3](#)), their effective aperture is fixed at the value of a single lens. Huntsman can, therefore, target fainter stars than SuperWASP and other similar systems, as its effective collecting area per target is larger (see [Figure 2.4](#)). These benefits, combined with Huntsman’s relatively cheap production due to its use of off-the-shelf lenses and detectors (compared to other large telescopes and their overall cost, see [Rauer et al. 2014](#) and [Ricker et al. 2015](#)), make Huntsman an efficient tool for detecting exoplanets around the brightest stars in the Solar neighbourhood.

2.1.2 The Advantages of Huntsman

As any ground-based facility, the Huntsman Telescope is subject to atmospheric effects that change during transits, scintillation, and systematic errors like telescope tracking, non-linearity of the detectors, and flat-fielding of the ubiquitous CCDs. Most of these noise sources can be mitigated by using a suitable observational strategy, but scintillation and photon noise are ultimately limited by the size of the telescope aperture, as shown in [section 1.2](#). I explain here how Huntsman minimises most of

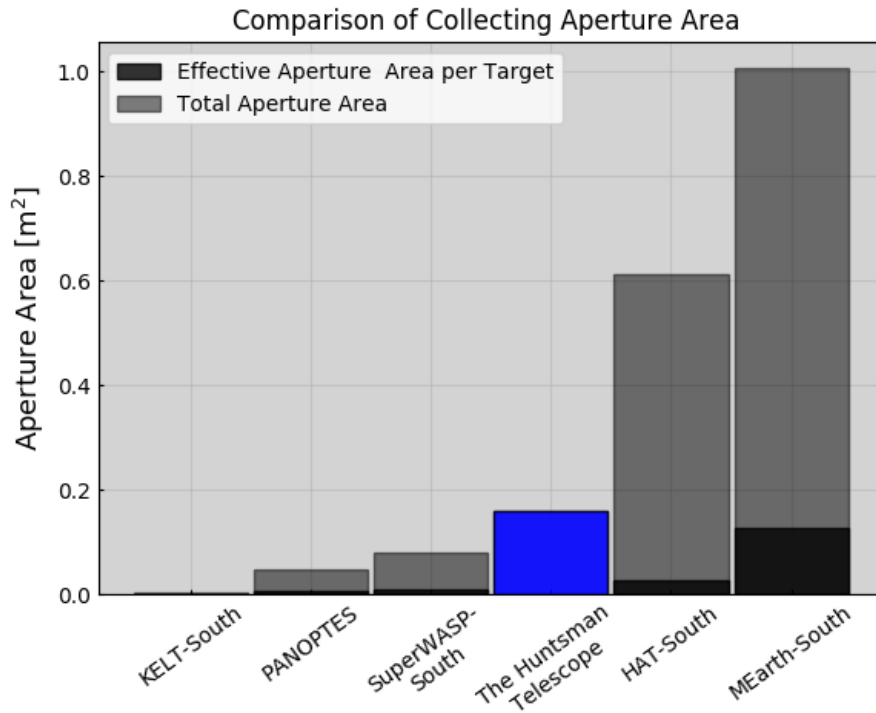


FIGURE 2.4: Aperture area per facility for various ground-based projects making observations of exoplanets. PANOPTES values are given by [Gee et al. \(2016\)](#), and the rest is extracted from [Law et al. \(2015\)](#).

these errors to achieve a good precision when observing bright targets, reducing at the same time the stray light within the telescope, and improving the pixel sampling.

Our main targets are relatively bright TESS stars (see [subsection 1.1.2](#) and [Barclay et al. 2018](#)), which are not limited by photon-noise due to their proximity to Earth. Instead, bright targets are scintillation noise limited ([Osborn et al., 2015](#)). As scintillation is inversely proportional to the telescope aperture, what we do is increase the effective aperture by using an array of lenses in order to keep scintillation noise to a minimum.

Telescopes are also affected by contamination caused by stray light. To mitigate this, small refracting telescopes, and high-quality telephoto lenses, are typically optimised for low scattering. They have unobstructed pupils and any reflected light travels backwards out of the path of the beam, which further reduces the amount of unwanted light inside the telescope. These optical systems often also have very low optical distortions and are very well baffled.

The Huntsman lenses are the latest generation of telephoto lenses by Canon, with excellent apochromatic qualities, extremely well baffled, and with a nano-fabricated coating on some of their internal components. This coating, driven by a sub-wavelength structure, has a continuous variation in the refractive index that helps to reduce stray light and ghosts. Other important features of the lenses

include a fully darkened interior, which absorbs any scattered light that does occur; and a lens hood that also helps to reduce scattered light from bright, nearby sources. The lenses have an unobstructed pupil, and therefore the Point Spread Function (PSF) of defocused stars will not be doughnut-shaped. This increases the signal and reduces the background noise. All of these characteristics make the Huntsman Telescope ideal to perform defocused photometry of bright targets.

With this in mind, Huntsman uses four front-illuminated full-frame CCDs with microlens arrays – SBIG STF-8300M cameras with a pixel grid of 3352×2532 pixels. The cost per CCD is approximately USD \$2,300, which can be considered cost-effective for a cooled CCD camera. Bigger CCDs and in particular professional back-illuminated devices are much more expensive, and price depends on cosmetic grade such as the number of bad pixels, quantum efficiency, readout noise, etc.

In all big optical instruments, $\sim 15 \mu\text{m}$ pixel CCDs are often standard ([Irwin et al., 2009](#), [Auvergne et al., 2009](#), [Borucki et al., 2010](#)). For typical back-illuminated CCD pixel sizes of 12-18 μm , long focal lengths are generally required in order to achieve fine sampling with small telescopes. Conversely, the $\sim 6 \mu\text{m}$ sampling of many front-illuminated CCD image sensors might be inconveniently small for larger instruments, requiring short effective focal lengths for fine sampling. So, are back-illuminated CCDs and larger pixel sizes worth the extra cost? Depending on the focal length of the telescope and the pixel scale, the main advantage is larger full well capacity, which means more dynamic range per exposure at fixed read noise levels.

In terms of sensitivity and dynamic range, a small pixel sensor with low readout noise can be just as good as a large pixel sensor with higher readout noise, provided the optics can deliver the desired pixel scale without too much trouble. With Huntsman, small pixels also provide a better match of the seeing with the pixel scale, and microlens arrays are used to concentrate more light onto the pixels, yielding an effective QE that reaches 56% (see [Table 2.1](#)).

However, despite that theoretically the transformation rate between photons and electrons (i.e. QE) should be the same throughout the detector, this is not the real situation and there are effects caused by the pixel position, known as pixel-to-pixel variations. Additionally, imperfections in the microlens arrays can alter the response of a single pixel over its own area ([Mahato et al., 2018](#)), resulting in large variations of the intra-pixel QE, which is a problem for high-precision photometry. Such a situation can be mitigated by defocusing the lenses and spreading the light over many pixels.

A good benchmark for photometry with Huntsman is the WASP ([Street et al., 2003](#)) project, an international consortium of eight academic institutions that comprises two robotic observatories;

	SuperWASP-South	Present Huntsman
Operated by	Consortium of eight Universities	Macquarie University
Effective Aperture	0.08 m ² (8 lenses)	Current Design: 0.08 m ² (5 lenses) Final Design: 0.16 m ² (10 lenses)
CCD Illumination	Back-illuminated	Front-illuminated
CCD Model	Andor Technology DW436	SBIG STF-8300M
CCD Cost	Approx. USD \$50,000	Approx. USD \$2,300
Pixel Grid	2048 × 2048	3352 × 2532
Pixel Size	13.5 μm	5.4 μm
Pixel Scale	13.7'' / pixel	2.8'' / pixel
Full Well Capacity	80000 e ⁻	~ 26000 e ⁻
Peak QE	QE > 90%	QE ~ 56%
Readout Noise	12 - 18 e ⁻	~ 9.3 e ⁻
Type of Lenses	Canon 200mm, f/1.8 telephoto lenses	Canon 400mm, f/2.8L IS II USM telephoto lenses
Mount Type	Equatorial fork	German Equatorial
Mount Company	Optical Mechanics, Inc.	Software Bisque Paramount
Model	Torus mount	MEII Robotic telescope mount
Photometry Precision	~ 1% (Christian et al., 2006)	~ 0.4% on Bright Targets (this thesis)
Field of View per optic	7.8° × 7.8°	2.6° × 2.0°
AΩ per optic	0.09 deg ² m ²	0.59 deg ² m ²

TABLE 2.1: Comparison between SuperWasp-South and the Huntsman Telescope. Information for SuperWASP-South extracted from [Pollacco et al. \(2006\)](#) and <https://wasp-planets.net/technical/>. For Huntsman we are using the SBIG camera STF-8300M, whose values can be obtained from publicly available sites like <https://www.astroshop.eu/astronomical-cameras/sbig-camera-stf-8300m>

SuperWASP-South at the South African Astronomical Observatory, South Africa, and SuperWASP-North at Roque de los Muchachos Observatory, Spain. Each WASP unit consists of an array of eight Canon 200 mm f/1.8 telephoto lenses provided with 2048 x 2048 CCDs, by Andor Technology. WASP is one of the leading projects in ground-based exoplanet photometry, with more than 100 exoplanets discovered during more than 15 years in operation ([Christian et al., 2006](#)). This facility uses back-illuminated CCDs with a large pixel size of 13.5 μm, which are significantly more expensive (≥USD \$50,000) than those of Huntsman (see [Table 2.1](#) for comparison). This makes the Huntsman

Telescope, which was funded by only Macquarie University, an exoplanet follow-up facility that can be upgraded at a relatively affordable cost.

This prompts the question, is it more advantageous having a telephoto lens of 400 mm focal length with a small pixel size $\sim 5.4 \mu\text{m}$ front-illuminated CCD (Huntsman), rather than one of 200 mm with a larger pixel size $\sim 13.5 \mu\text{m}$ back-illuminated CCD (SuperWASP)? Since 200 or 400 mm are very short focal lengths for a telescope, Huntsman needs some of the smallest pixels around to get a finer pixel scale of $2.8''/\text{pix}$ compared to a coarse pixel scale of $13.7''/\text{pix}$ like in SuperWASP. This means using front-illuminated CCDs, as Huntsman does. A drawback of front-illuminated CCD devices is that they are less sensitive than others, they have lower quantum efficiency and relatively high readout noise.

Lenses of the same aperture with longer focal lengths like 600 mm, or even 800 mm allow for more options for detectors, and more freedom to choose pixel size and corresponding angular pixel scale. That means, however, bulkier lenses and more expensive detectors. With Huntsman, the fine sampling provided by the small pixel detector is ideal for using defocused photometry, as it means that much less defocusing of the lens is required to average over the pixel-to-pixel non-uniformities. At the same time, a small defocusing means a lower background noise within the aperture (see Chapter 4), as well as fewer blends with background stars when compared to a system with larger pixels (in arcsecs on sky).

3

Methodology

The Huntsman Telescope is still undergoing commissioning and is not yet automated. Recurring hardware problems, like persistent problems with the telescope guiding, a failing dome shutter, and insects destroying some of the electronics, while mostly solved now, severely limited the amount of data I was able to collect for this thesis. The detection of exoplanets with Huntsman needs optimal functionality of the telescope, and reliable robotic operation. This required us dealing with various types of bugs and difficulties in the instrument set-up stage. Solving these issues permanently will allow us to improve the performance of Huntsman in the future.

In this Chapter I describe how the Huntsman Telescope works, and the main strategies used when observing with Huntsman. I also discuss the methodology used to collect data, give a summary of the observations made during the time of this thesis, highlighting the main observational problems I had to overcome. Finally, I will describe the reduction of Huntsman data to prepare it for the photometric analysis explained later in Chapter 4.

3.1 The Huntsman Telescope in Operation

The operation of the Huntsman Telescope can be divided into two parts: 1) the mount and observatory dome, and 2) the Huntsman optical hardware, including cameras, lenses, and supporting equipment. Firstly, Huntsman uses a Software Bisque Paramount MEII¹ robotic telescope mount (see Table 2.1) which provides a proprietary software, TheSkyX Professional² from Software Bisque, to control both the mount and the dome. Secondly, for the optical components of Huntsman we use a

¹<http://www.bisque.com/sc/pages/ParamountMEII.aspx>

²<http://www.bisque.com/sc/pages/TheSkyX-Professional-Edition.aspx>

software that has been tested and developed for the PANOPTES³ project: the PANOPTES Observatory Control System (hereafter POCS, [Gee et al. 2016](#)), which is an open source Python 3 library that runs an automated observing scheme. The adaptability and customisation of POCS made it ideal to control the Huntsman Telescope⁴.

Before any observations were made, the hardware was assessed and power-cycled if necessary, before TheSkyX was initialised. POCS was then initialised. As this was still during daylight, POCS automatically put the telescope and dome into sleep mode and waited until astronomical twilight to commence observations of the first target of the night. When the telescope was ready to observe a target, POCS determined an optimal target from a prioritised target list and directed the mount to slew to the required coordinates. In each observational run, the mount and telescope were controlled via POCS by using a control computer. Each optical system (i.e. lens + CCD) was managed via a Raspberry pi computer, and initialised from an individual server.

To guide the mount, Huntsman uses the autoguider software provided by TheSkyX, which has to be set up manually by taking a photo of the guide field and selecting a guide star. This has to eventually be checked later each night to assess if the guiding of the telescope is optimal. If the autoguider presents problems, we need to remove the guide star, take another photo of the field, and then initialise the guider again with TheSkyX to auto-find the guide star. All these steps are being automated for future autonomous operation of the facility.

3.1.1 Collection of Data

For this thesis, four data sets were collected, and all their characteristics are tabulated in [Table 3.1](#). The primary goal during the time line of this thesis was to determine the optimal on-sky photometry precision we can obtain with the Huntsman Telescope. The collected data also served as a test for studying the different components of the HUNtsman PHOtometry Pipeline (HUPHOP), developed to do the photometric analysis (see [section 4.5](#)).

Our main targets for this photometry commissioning are bright stars, which are suitable for continuous follow-up from ground-based facilities like Huntsman. As described below, the ideal range of stellar magnitudes for Huntsman is 8-12 mag in the Johnson System, which is also where most TESS candidates are expected to be discovered (see right-hand panel of [Figure 1.2](#) and [Figure 3.2](#)). Also, the smaller the telescope is, the more valid the Young approximation given by [Equation 1.1](#) is,

³<https://projectpanoptes.org/>

⁴The adaptation of POCS to Huntsman can be checked at <https://github.com/AstroHuntsman/huntsman-pocs>

	Observational runs			
	2018-08-01	2018-09-13	2018-09-18	2018-11-25
Active Cameras	1	2	4	4
Filter used	G band	G band	G band	G band
Number of Exposures	170	49	58	171
Exposure time [sec]	10	45	45	10
Field	Wasp 20	HIP 65	HD 224822	TYC 8540-01203-1

TABLE 3.1: Report of observations made with Huntsman. The CCDs in this table are the SBIG STF-8300M. Due to delays in commissioning the facility, these were the only nights where I was able to collect high-quality data.

so in the aforementioned range of magnitudes we can apply the ratio depicted in Figure 1.5. For a deeper discussion of scintillation and photon noise, the reader can refer to section 1.2 and references therein.

One of the first things we need to be aware of when observing bright targets is the full well capacity of the pixels in our detector, so that saturation is not reached. The first basic step with Huntsman is to know how long the exposure time should be in order to have a significant number of counts in our detector pixels, which will directly depend on the magnitude of the target star and the size of the PSF. For the target stars observed for this thesis, exposure times from 10 to 45 s were adopted, which produced good signal-to-noise without saturation.

The four successful observational runs performed with Huntsman during this thesis are reported in Table 3.1. The main issue with most of these observations is the presence of time intervals during which no data was collected, or gaps, that made it difficult to obtain a clear estimate of the on-sky photometry precision of Huntsman (see Appendix). This happened due to many issues with the software and hardware which interrupted observations. As an example of a problem we had, close to midnight on the 1st of August 2018 a ladder inside the dome fell over, and mechanically blocked the movement of the mount. This caused us to stop the observations for about 40 minutes, while someone on site removed the obstacle, so we could resume remote control again.

An exception to the above was the 18th September 2018, where the data was continuous for the whole observation. For all of the observations the same filter was used, a Sloan g-band filter (Fukugita et al., 1996) from Astrodon. Figure 3.1 shows the transmission properties of four Sloan filters⁵ that Huntsman can eventually use; g' is the one used during the course of this thesis, centred at about 480

⁵More specifications of these filters can be found at <https://farpointastro.com/shop/astrodon-photometrics-sloan-filters/>

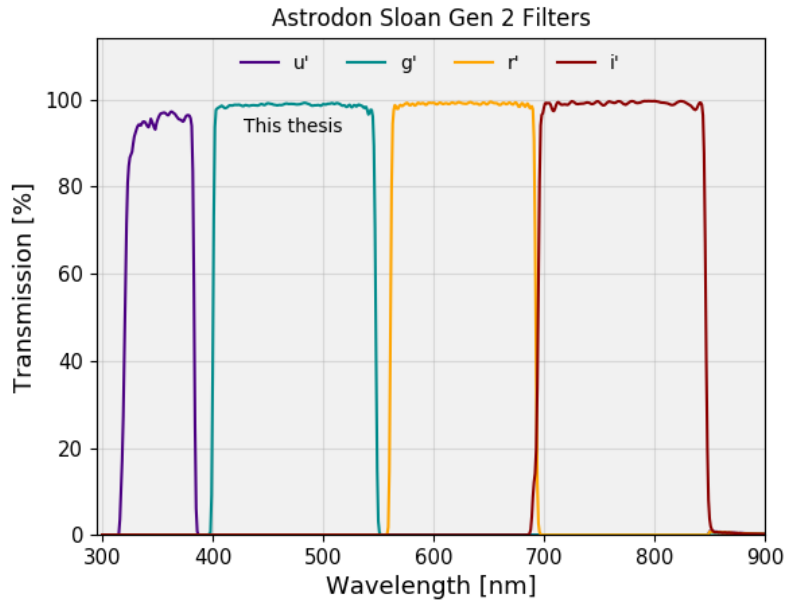


FIGURE 3.1: Transmission curves of Sloan second generation filters. The Huntsman Telescope uses a Sloan g' 2 round filter. The data of this plot was taken by Adam Joyce at Macquarie University, using a spectrophotometer Cary 5000 UV-Vis-NIR.

nm. In the next few months an upgrade of the filter wheels of Huntsman will be carried out, and observing with multiple filters during a single observational run will be possible. Huntsman lacks filter wheels at the moment and that is the reason I used just one filter for this thesis, and it was g' due to the observational program of other team members, so that it was an advantage for all of us. An optimal observation should be done with a filter towards redder wavelengths, where most of the atmospheric absorption is avoided (e.g. r' in [Figure 3.1](#)).

For the analysis of the photometric precision of the Huntsman telescope in [Chapter 4](#), the data set taken on 18 September 2018 from four active Huntsman cameras is adopted, which presented no technical issues. The fifth camera (attached to the RASA telescope, see [Figure 2.2](#)) was not used as it is not configured yet. Other data sets were collected over the course of this thesis, but most of them were disregarded, as they presented bad telescope guiding besides the gaps mentioned before; this was not ideal to give a reliable estimate of the photometric precision of the telescope (see [Appendix](#)).

Furthermore, in the night of the 18th September 2018, the Huntsman camera 83F010774 was defocused, allowing us to do a side-by-side comparison of the achievable precision by contrasting the photometric precision obtained from a defocused camera with the other three in-focus cameras. Such a comparison will be shown in [section 4.5](#). For this and other nights, the targets were selected by following the distribution of TESS bright stars shown by [Figure 3.2](#).

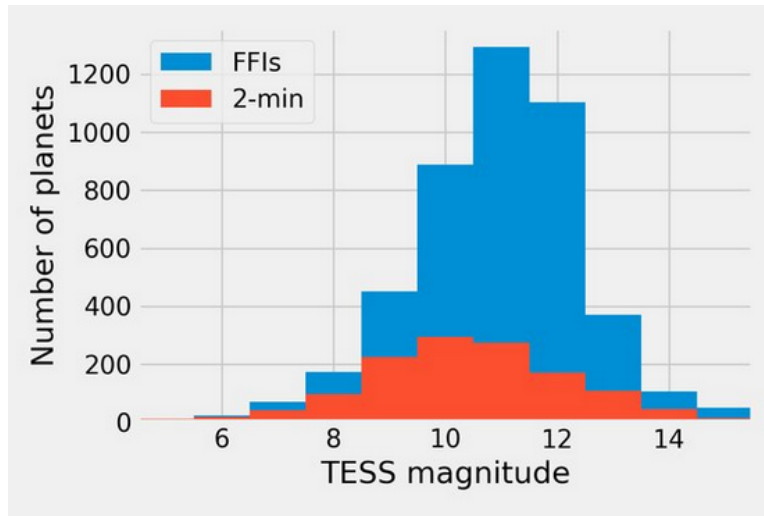


FIGURE 3.2: Magnitude of the target stars as measured through the TESS filter. TESS stars show a median magnitude of 10.4, extending down to 3.3 and up to 15.3. This is the range of stellar magnitudes where most TESS exoplanet candidates will be found. Source: [Barclay et al. \(2018\)](#)

3.2 Characterising Huntsman CCDs

To achieve high-precision photometry with the Huntsman Telescope, we need optimal functionality from all of the hardware components. In particular, the response of the CCDs to the light is crucial, as any imperfection can cause detrimental effects in the collected data. In this section is measured the linearity of Huntsman CCDs, in order to analyse if any additional corrections should be performed once the data is collected (e.g. to account for non-linear effects).

To determine the linearity of Huntsman CCD detectors, various measurements were performed at several exposure times, using the SBIG STF-8300M cameras under controlled conditions. These images were taken during daylight inside the dome, with the CCD temperature ranging from -1.8° to 0.3° C. The cameras were pointing towards the floor of the dome when taking the exposures. Although the illumination pattern was not perfectly flat, the ambient light during the data was stable, homogeneous, and sufficient for measuring linearity. The integration times were between 1 and 65 seconds with two different step sizes: every 5 s from 1-31 s, and every 2 s from 31-65 s, to cover the full dynamic range of the CCDs. The experiment was repeated five times to build up good statistics.

Unlike the gain factor, G , the readout noise was not characterised for each CCD but taken from the manufacturer's data sheet. This can be part of a future refinement for a better estimation of the Huntsman precision; however, for a typical observation we expect the readout noise to contribute only insignificantly to the overall noise.

The linearity data with and without bias correction was analysed, and we found that such a

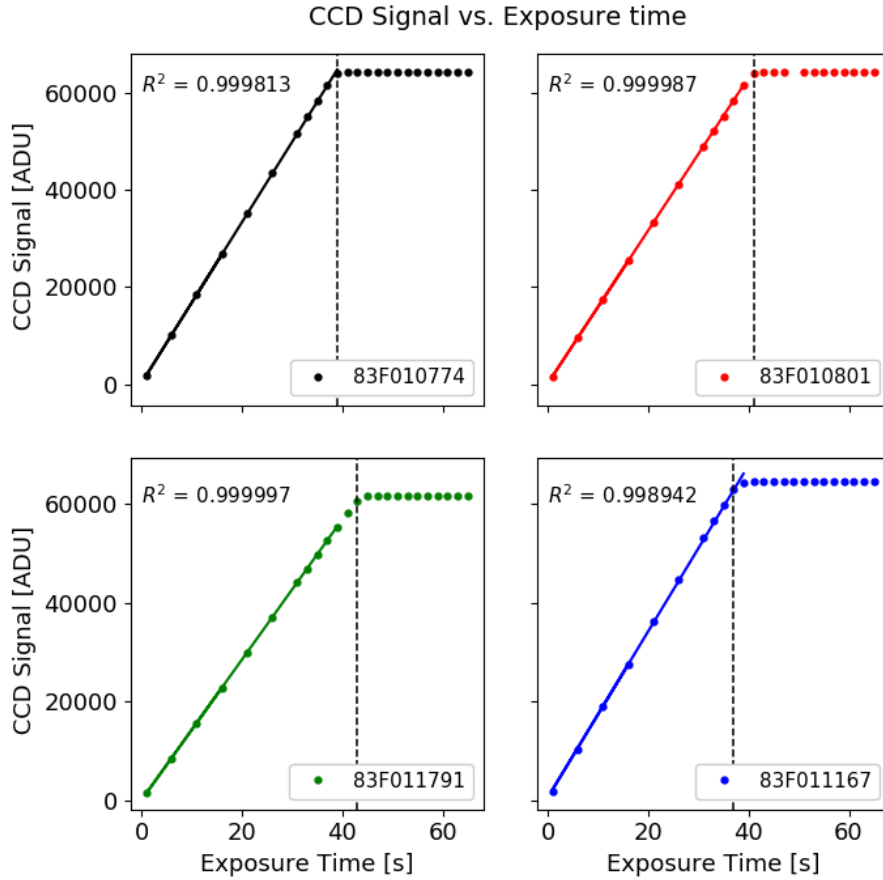


FIGURE 3.3: Signal in the Huntsman CCDs as a function of exposure times. These plots were used to study the linearity of the four Huntsman CCD SBIG STF-8300M detectors. Data includes bias correction. Each dot is the mean value for a rectangular area of 500×500 pixels. The coefficient of correlation for the linear fit (R^2) between predicted (solid lines) and measured (filled dots) CCD signal, is shown in each plot. The dashed vertical line in each plot represents the exposure time when the CCD reached saturation.

correction was unimportant (i.e. a difference of less than 0.001%), for the range of CCD temperatures and exposure times used in these tests. As the illumination was not flat, a box of 500×500 pixels was selected from each frame, and its mean value was computed (this was called the CCD Signal). In Figure 3.3 the resulting linearity data for each CCD is plotted (i.e. CCD Signal vs. Exposure Time), where the linear fit and its coefficient of determination are shown. For all CCDs, the coefficient is about 99.9%, indicating a nearly-perfect linearity for the detectors before saturation is reached at ~ 65535 counts.

The images taken during daylight inside the dome were also used to compute the gain of the Huntsman CCDs. After applying the bias correction to these images, the signal (S) on each pixel can be represented in terms of the noise (N) by Poisson statistics, as $S = N^2$. Since the gain (G) relates electrons and “counts” measured on a CCD, this expression can be rewritten as $GS' = (GN')^2$ so that

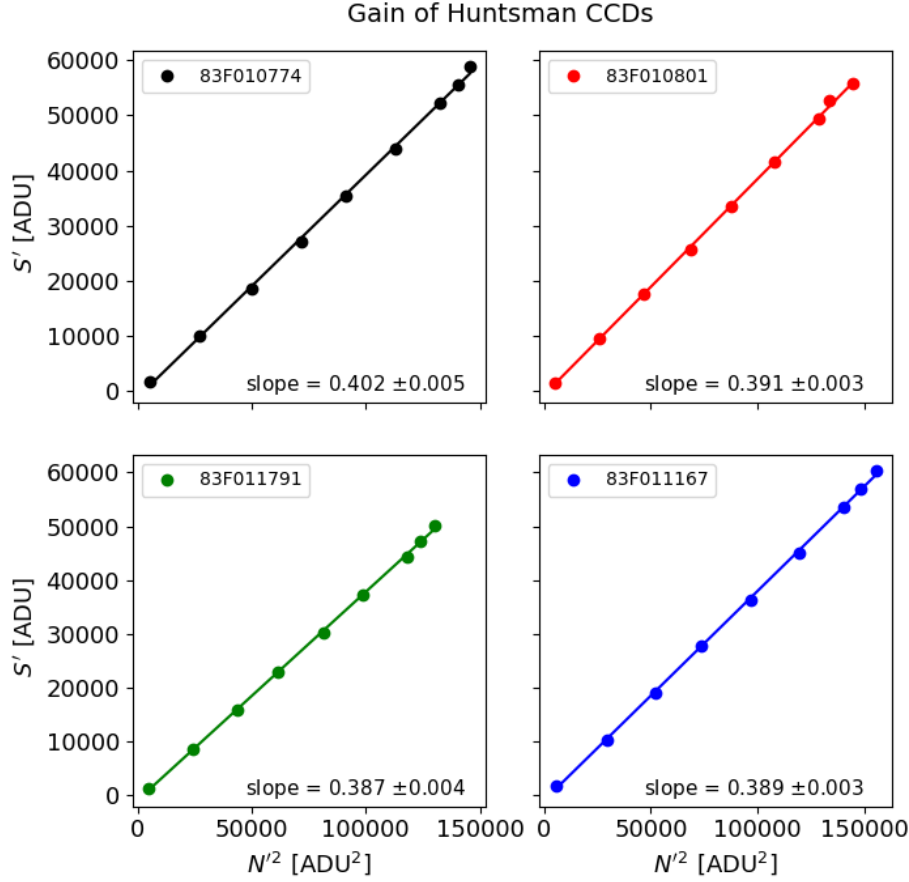


FIGURE 3.4: Signal as a function of the variance of the measured counts (defined as $\sigma^2/2$). The gain of each CCD is computed from the slope of the linear fit. All the values are reported in Table 3.2 along with the deviation from the nominal value given by the manufacturer.

finally we have $S' = GN'^2$.

If we measure both the signal (S') and the noise (N') in Analog-to-Digital Units (ADUs), for different signal levels (i.e. exposure times), the slope of the fit will be G . To estimate the gain in each camera, the following steps were performed:

- The average of images with the same exposure time was taken to find an *averaged image*.
- The difference of images with the same exposure time was computed to find a *subtracted image*.
- A box of 400×400 pixels² was defined on a homogeneous region of both the averaged and subtracted images.
- The mean value inside the box of the averaged image was taken, and defined as the signal (S'). The standard deviation σ inside the box of the subtracted image was found too.

Once the previous four steps were conducted, the *variance* of the measured counts was defined as $N'^2 = \frac{\sigma^2}{2}$, and finally S' vs. N'^2 was plotted as in Figure 3.4. The results of the computed gain for each Huntsman CCD, together with the deviation from the nominal value given by the manufacturer, are tabulated in Table 3.2.

CCD Detector	Computed gain [e^-/ADU]	Deviation
83F010774	0.402 ± 0.005	8.75%
83F010801	0.391 ± 0.003	5.68%
83F011167	0.389 ± 0.003	5.14%
83F011791	0.387 ± 0.004	4.59%

TABLE 3.2: Measured gain of four active Huntsman SBIG STF-8300M cameras. The deviation is computed with respect to the nominal gain given by the manufacturer (i.e. $G = 0.37 e^-/\text{ADU}$), which was obtained from <https://www.astroshop.eu/astronomical-cameras/sbig-camera-stf-8300m>

3.3 Data Reduction

All of the FITS data taken during an observation is in a *raw* state and must be calibrated before it can be worked with. This process is known as *data reduction* and is summarised in Figure 3.5. For the Huntsman Telescope, I have written a CCD Data reduction pipeline using Python 3, and an affiliated package of [Astropy Collaboration et al. \(2013, 2018\)](#), `ccdproc` ([Craig et al., 2015](#)), which contains many functions used to do basic reductions of astronomical data. This reduction pipeline for Huntsman performs bias subtraction, flat-fielding correction, and masking of bad pixels. Dark correction has been neglected given the short exposure times used in this thesis, and the low dark current of Huntsman CCDs ($0.15 e^-/\text{pix/s}$) when compared to the readout noise ($\sim 9.3 e^-$)⁶. In the following, there is a brief outline of how the reduction of data is usually done in observational astronomy.

3.3.1 CCD Noise and Bias Subtraction

A CCD has a minimum noise level associated with its electronics. Variations in the signal offset in the readout electronics (readout noise), electrons created independently of the light falling on the CCD due to thermal currents (dark current), and the noise introduced because of the conversion of accumulated charges into ADUs, all produce a background noisy signal.

⁶See <http://diffractionlimited.com/product/stf-8300/>

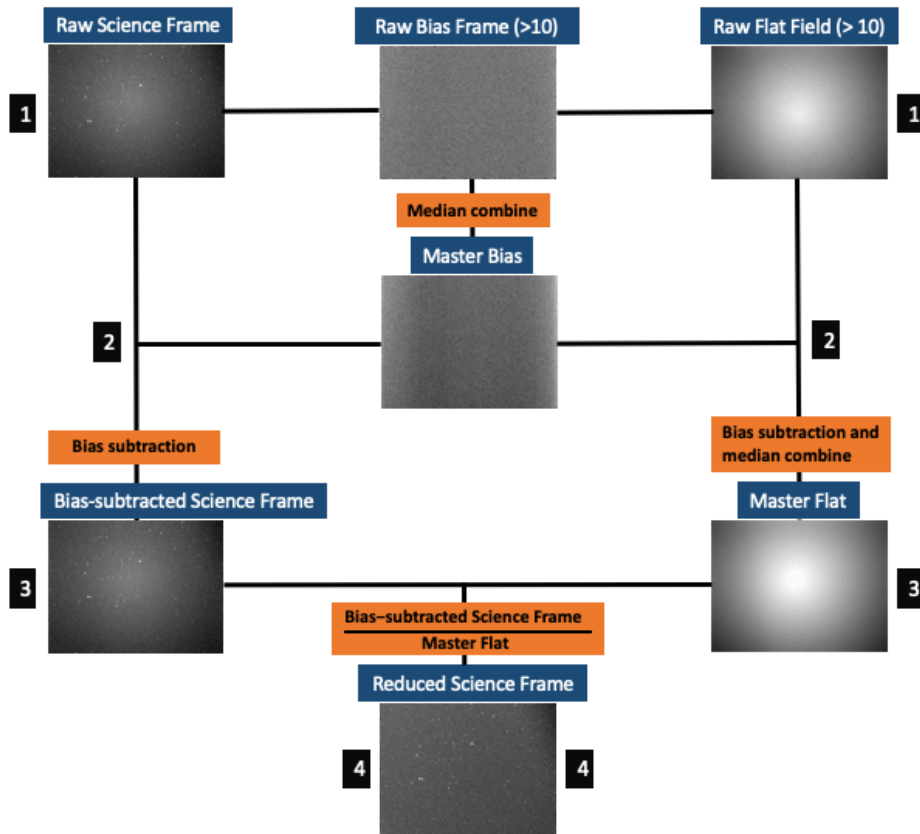


FIGURE 3.5: Scheme of CCD data reduction for the Huntsman Telescope. Level 1 is the collection of raw data during an observational run, including science frames, bias frames, and flat fields. Level 2 is the creation of a Master Bias. Level 3 is the bias subtraction from science frames and flat fields. After the bias subtraction the Master Flat is also created. Finally, Level 4 is what we call flat-fielding correction, where we divide the bias-subtracted science frame by the Master Flat, and we then obtain the final output image. In this last step, a bad pixel masking is also applied, and the final output image is used to perform the aperture photometry.

Also the CCD electronics produce a signal offset called the Bias level, which is required to ensure the internal Analog-to-Digital converter always receives a positive voltage; this signal offset needs to be removed. To do this, we need to take a significant number of bias frames (>10) during each observation night (this corresponds to level 1 in Figure 3.5), with an exposure time of zero seconds and the camera shutter closed,. Once we have the bias frames, we (median) combine them into one frame known as the Master Bias (Level 2), and this one will be subtracted from all the science frames and flat fields (Level 3).

3.3.2 Flat-Fielding Correction

Science data often presents uneven light distributions, or gradients arising due to a non-uniform illumination across the CCD by the optical system. There can be many causes giving rise to signal variations across pixels, such as fluctuations in the pixel-to-pixel or intra-pixel sensitivity, dust particles

in the optics, and optical vignetting. To correct these artifacts, we need some uniformly-illuminated images known as *flat fields*. These are collected by exposing the detector to a uniform light source such as the sky during astronomical twilight (evening/morning flats). Multiple flat fields are needed to suppress noise, and once we are taking flats at both dawn and dusk, we will be able to remove sky gradients as well. These flat fields are then (median) combined into a Master Flat, which is used to divide the bias-subtracted science images (see level 3 and 4 in [Figure 3.5](#)).

3.3.3 Bad Pixels Correction

Each of Huntsman’s CCDs has some pixels that do not respond properly to the amount of light falling onto them. If a CCD is exposed to a light source and some pixels do not record the photons when they strike the detector, these are called *dead pixels*. On the other hand, some pixels exhibit an anomalously high dark current and their potential well is totally full, and these are called *hot pixels*. With the aim of avoiding both types of bad pixels in the photometric analysis that will be explained in Chapter 4, we need a *bad pixel mask* for each camera, where we can identify the bad pixels in order to mask them from the data. To do this, the approach used in Huntsman’s pipeline is to look at a pixel counts histogram of a master bias frame for a given night. In this type of frame the shutter is closed, so we can identify those pixels with high counts which are outliers of the distribution, and then create a first mask for the hot pixels. Subsequently, we use a Master Flat where the illumination is uniform during a significant exposure time, such that most of the pixels should have recorded a signal, and those which do not record a signal that scales with the exposure time are masked, thus creating a second mask for the dead pixels.

We now combine both masks into a *bad pixel mask* that is used to avoid the bad pixels. Using this *bad pixel mask* we designed a filter that surrounds each bad pixel with a box of 3×3 pixels, so that each bad pixel remains in the centre of a sub-array, and then we replace it by the median of the surrounding box, excluding the bad pixel. This filter was written in Python 3 and included in the data-reduction pipeline of Huntsman. There are some generic filters already implemented in some libraries of *Astropy*, but in computational terms these are too expensive as they make a filter over all pixels of the CCD. The filter designed for Huntsman’s reduction pipeline is fast and effective, as it just looks for the specific coordinates of each bad pixel to replace that pixel only, and leaves the remainder of pixels with their originally recorded counts.

4

Photometry Results

Having calibrated the science frames, the next step is to extract and analyse the target light curve data. In this Chapter, I introduce the aperture photometry used in this thesis to study the temporal variations of stellar flux, as well as the main problems I had to address for its correct implementation. Briefly, an area on the CCD that contains the light from the star is defined, known as an aperture, which will have a specific shape (e.g. rectangular, circular, elliptical, etc.). All the counts (photons) in the pixels within the aperture are then summed up to have a net integrated count (total flux) associated to the object for a given exposure. As shown below, there is an advantage of working with circular apertures to cancel any residual gradient present in the sky background of Huntsman imaging.

4.1 Aperture Photometry

Aperture photometry is a common task in astronomy. For the purpose of this work I chose individual sources by hand, which was more accurate and instructive than using completely automated methods. There are various software packages to perform aperture photometry, including Photutils ([Bradley et al., 2018](#)) from Astropy Collaboration et al. (2013, 2018), Price-Whelan et al. (2018), SExtractor ([Bertin & Arnouts, 1996](#), [Holwerda, 2005](#)), and AstroimageJ ([Collins et al., 2017](#)). To fully weigh the upsides and drawbacks of the method, I have designed a custom photometry pipeline based upon Photutils and Astropy that will be introduced in [section 4.5](#).

An important element to perform high-precision photometry with Huntsman, is the correct subtraction of any light source in the data that is not originated from the object of interest. This can include nearby objects that can be avoided or masked. One source of such a noise more challenging to quantify and subtract is the *sky background*, which includes the terrestrial night sky emission. Therefore, to work with Huntsman data we must accurately find the background’s signal and remove

it from that of the target star, so we only have starlight without any contamination.

The sky background can be determined by centring an annular aperture on the target star to derive a local approximation of the sky brightness. In other words, this is the signal we would measure if the star was not on a particular region of the detector. The aperture needs to be symmetric in order to cancel out any gradient that might be present in the background. The inner and outer radii of the annulus determine the accuracy of the background estimation. The inner radius of this annulus is chosen large enough to exclude any contribution from the source, but still close enough to measure the local sky level (Da Costa, 1992). The outer radius is small enough to keep the local background estimation representative for the source, but still containing a large number of pixels to make a precise measurement of the sky.

Once the annular aperture is defined, we compute an approximate value for the average sky counts per pixel by examining the distribution of pixel intensities within the annulus. There are three possible options: *mean*, *median*, or *mode* (Kendall & Stuart, 1977), and the one to be used depends on how contaminated our background is by the sky signal and the wings of the stellar PSF. If we find a symmetric histogram of the pixel values, we use the mean or the median to represent a typical value. With skewed histograms, where the wings of the stellar PSF contribute to the local background (e.g. for bright stars), the *mode* which is the peak value of the histogram would be the optimal estimate for the signal of the sky background. For the Huntsman observations, and after careful examination of the histograms, we found a mean worked sufficiently well since the sky level pixel distribution was nearly symmetric about the mean.

Finding the exact centroid of the target star is also an important measurement to achieve high photometry precision. To this end, a two-dimensional Gaussian function `centroid_2dg` from `Photutils` (Bradley et al., 2018) was used, avoiding fields that were crowded with other sources.

4.2 Differential Photometry

There are various techniques to achieve high-precision photometry including telescope defocusing (Southworth et al., 2009a, Mann et al., 2011, Croll et al., 2011, Fukui et al., 2016, Zhao et al., 2014), the use of orthogonal CCDs (Johnson et al., 2009, 2010), narrow-band spectrophotometry with tunable filters (Colón et al., 2012), and lately an effort to use diffusers (Stefansson et al., 2017). The telescope defocusing technique was explored in the framework of this thesis, as described in the next section.

In exoplanet transit photometry, we compare a target star’s flux Φ_T , to the sum of the flux of one

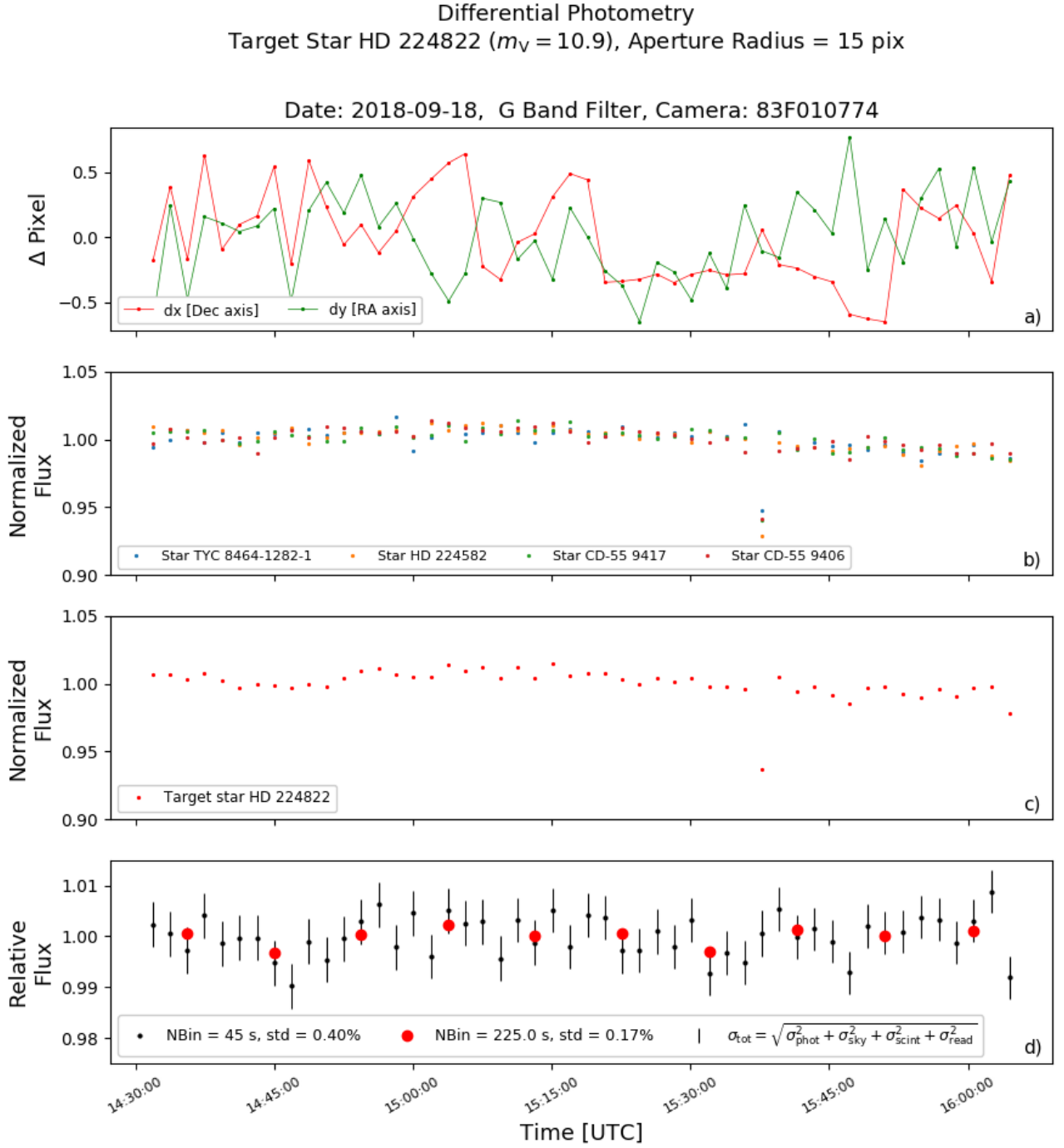


FIGURE 4.1: *Panel a):* Variation of the target star's centroid position for both the right ascension (green line) and declination (red line) axes. The aperture radius is set to 15 pixels (extracted from Figure 4.2). *Panel b):* Normalised flux for each of the reference stars. *Panel c):* Normalised flux of the target star (i.e. aperture photometry of HD 224822). *Panel d):* Differential flux of the target star HD 224822 respect to the integrated flux of the ensemble of reference stars. Both the binned (red dots) and the unbinned data (black dots) were plotted. The error bars correspond to the amplitude error caused by photon, sky background, scintillation, and readout noise. The data set of this plot was collected on 18 September 2018, using an exposure time of 45 s. This plot contains the data of a single Huntsman camera (83F010774). The lens was defocused to obtain a Full Width at Half-Maximum (FWHM) of the PSF of ~ 30 pixels, and a G band filter was used.

or more stars that are in the same FOV. The ensuing quantity is the so-called *relative* or *differential* flux. This differential photometry is the standard technique to detect any subtle brightness variations on a specific star. The stars we use to compare the flux of the target star are named *reference* or *comparison* stars, with flux Φ_r . A fairly compact ensemble of reference stars helps to reduce the error in the measurements caused by the angular correlation of scintillation (Gilliland et al., 1993, Kornilov, 2012). Therefore, for this thesis the reference stars were selected close to each other. For n reference stars, the measured differential flux is computed:

$$\Phi_{\text{relative}} = \frac{\Phi_T}{\sum_r^n \Phi_r} \quad (4.1)$$

The left-hand side of Equation 4.1 is dimensionless, and is what is plotted as a flux time series of a target star. The resulting “light curve” (see Figure 4.1) is the primary measurement objective when searching for any exoplanet transient event (e.g. a transit). A distinct advantage of this method is that any small dips in flux due to shifting cloud cover (section 1.2) will likely impact both the target and reference stars in a similar way. When the ratio of the two is taken, as they are subject to the same external variations on their measured flux, such effects cancel and the underlying exoplanet transient event can be isolated.

Figure 4.1 shows four important parameters to do optimal photometry. The guiding error of the telescope for this data set is illustrated in panel (a). It is worth noticing that the centroid of the star keeps changing its position on the CCD. Here the positional drift is not significantly high (i.e. less than a pixel), which is ideal for high-precision photometry, as the light of our star is dwelling nearly in the same spot of the CCD. This is important because having the light in the same location of the detector help us to reduce the noise due to pixel-to-pixel variations and flat-fielding errors. The panel (b) corresponds to the normalised flux of each of the four reference stars, illustrating their relatively stable fluxes with time. This guarantees that we have reference stars that are not subject to significant intrinsic variations on their flux, which is an essential and important detail to check. In addition, the reference stars were carefully selected from similar spectral types, in order to minimise differential extinction (see section 1.2).

Panel (c) in Figure 4.1 shows the aperture photometry flux for the target star. By comparing this panel and the reference stars in panel (b) we can note that at $\sim 15:40:00$ [UTC] there is a variation in all the fluxes. This is probably a transparency variation likely due to clouds, which affected the same portion of the image in a similar way. The differential photometry is contained in panel (d), where the flux of the target star is divided by the integrated flux of the reference stars, and normalised using the

mean of the light curve. We can see how the differential flux ratio gets rid of this type of variation, which illustrates nicely why we always use reference stars when observing from the ground.

4.3 Signal-to-Noise and Aperture Radius

The signal-to-noise ratio (S/N) is a dimensionless quantity and important concept in photometry. This section contains the equations to compute S/N , and an explanation of how this ratio was used to find the optimal aperture radius for the photometric analysis of Huntsman data. There are three main noise sources, including that of the target star, the sky background, and the readout of the CCD. For the computation of S/N we exclude the scintillation noise.

The signal is the total number of photons from a target object. This contribution reflects a rate of photons collected in a certain amount of time and therefore has random variations in the number of photons striking our detector each second, which is known as *photon noise*. The amplitude error of this quantity is well characterised via the Poisson statistics, and for a given exposure time t_{exp} , the signal of the target, S_{phot} , and its associated Poisson photon noise, N_{phot} , are given by:

$$\begin{aligned} S_{\text{phot}} &= t_{\text{exp}} R_{\star} G, \\ N_{\text{phot}} &= \sqrt{t_{\text{exp}} R_{\star} G}, \end{aligned} \tag{4.2}$$

where R_{\star} is the rate of counts per second from the target star [ADU/s], and G is the gain [e^- /ADU] of the CCD being used¹.

The contribution of the sky background signal, S_{sky} , and its corresponding Poisson noise, N_{sky} , is :

$$\begin{aligned} S_{\text{sky}} &= t_{\text{exp}} n_{\text{pix}} R_{\text{sky}} G, \\ N_{\text{sky}} &= \sqrt{t_{\text{exp}} n_{\text{pix}} R_{\text{sky}} G}. \end{aligned} \tag{4.3}$$

There is also a noise contribution from the readout of the CCD known as *readout noise*:

$$N_{\text{read}} = R_{\text{read}} \sqrt{n_{\text{pix}}}. \tag{4.4}$$

In the last two equations n_{pix} is the number of pixels within the aperture, R_{sky} is the number of counts per second per pixel in the sky background [ADU/s/pix], and R_{read} is the readout noise of the detector in electrons per pixel [e^- /pix].

¹We take the values computed in [section 3.2](#), and reported in [Table 3.2](#)

By following a similar formalism to that of [Howell \(1989\)](#), the S/N for the measured flux of a single star used with Huntsman data is derived from the CCD equation, as follows:

$$S/N = \frac{R_{\star} \sqrt{t_{\text{exp}} G}}{\sqrt{R_{\star} + n_{\text{pix}} \left(R_{\text{sky}} + \frac{R_{\text{dark}}}{G} + \frac{R_{\text{read}}^2}{t_{\text{exp}} G} \right)}}. \quad (4.5)$$

The additional term R_{dark} in [Equation 4.5](#) is the dark current given in electrons per second per pixel [$e^-/\text{s/pix}$]. For many modern CCDs used in astronomy, like those in the Huntsman Telescope, this term can safely be assumed as $R_{\text{dark}} \approx 0$ when calculating S/N^2 . Therefore, the final equation for S/N is given by,

$$S/N = \frac{R_{\star} \sqrt{t_{\text{exp}} G}}{\sqrt{R_{\star} + n_{\text{pix}} \left(R_{\text{sky}} + \frac{R_{\text{read}}^2}{t_{\text{exp}} G} \right)}}. \quad (4.6)$$

When we are object limited (i.e. $R_{\star} \gg R_{\text{sky}} + R_{\text{dark}} + \frac{R_{\text{read}}^2}{G}$), S/N is simply $\sqrt{t_{\text{exp}} R_{\star} G}$ – we can see that the number of photons collected per exposure ultimately limits our achievable precision. However, the atmospheric conditions of Huntsman’s location are unexceptional, and Huntsman’s detectors are not perfectly noise-free.

In addition to the above, as we have a reference brightness from an ensemble of reference stars, the photometric precision of our measurements should be correctly calculated for all of them. In terms of the ensemble integrated signal of n reference stars, S_{ensemble} [e^-/s], the numerator in [Equation 4.1](#) can be written as,

$$S_{\text{ensemble}} = \sum_r^n t_{\text{exp}} R_{\star,r} G, \quad (4.7)$$

where $R_{\star,r}$ is the total sky-subtracted counts per second [ADU/s] of each reference star r . Using this expression, the S/N for an ensemble of stars, S/N_{ensemble} , is

$$S/N_{\text{ensemble}} = \frac{\sum_r^n R_{\star,r} \sqrt{t_{\text{exp}} G}}{\sqrt{\sum_r^n R_{\star,r} + n_{\text{pix},r} \left(R_{\text{sky},r} + \frac{R_{\text{read}}^2}{t_{\text{exp}} G} \right)}}. \quad (4.8)$$

Combining both the signal-to-noise ratio of the target star, S/N_{target} , determined with [Equation 4.6](#), and that of the ensemble, S/N_{ensemble} (see [Equation 4.8](#)), we can find the signal-to-noise ratio for differential photometry adopting Equation 6 from [Deeg \(2013\)](#),

²For a Huntsman CCD, $R_{\text{dark}} \sim 0.15 \text{ e}^-/\text{s/pix}$ at 0° C , as extracted from <http://diffractionlimited.com/product/stf-8300/>

$$S/N_{\text{diff}} = \frac{1}{\sqrt{S/N_{\text{target}}^{-2} + S/N_{\text{ensemble}}^{-2}}}. \quad (4.9)$$

From the last equation we can see that we need approximately as much combined flux from the ensemble of reference stars as from the target, in order to avoid limiting the signal-to-noise of the differential photometry below the value achievable on the target star. If the photometry is performed without an ensemble of reference stars, Equation 4.9 becomes S/N_{target} , which is called simple aperture photometry.

4.3.1 Selection of Optimal Aperture

The selection of an optimal aperture balances collecting all the light of our target star, with collecting too many low signal-to-noise pixels, with introducing too much noise. To find the optimal aperture we compute S/N_{diff} ³ for a range of aperture radii (i.e. 0.8 - 25 pixels), and find where S/N_{diff} peaks. This peak occurs at the radius where the signal from the target star dominates over the noise of the background. This is expressed mathematically in Equation 4.6, which decreases inversely with n_{pix} : beyond the optimal aperture, the combined contribution (in the denominator) of photon noise, sky background, and CCD readout starts to overpass the signal of the object (in the numerator).

For the practical determination of S/N_{diff} , the signal was background subtracted and the noise was estimated from the total contribution of photon noise, sky background, and readout noise. S/N_{diff} from each frame is calculated using Equation 4.9, and we have then an averaged S/N_{diff} from all frames.

In the upper plot of Figure 4.2 is shown the standard deviation of light curves with different aperture radii. The target star was HD 224822 ($m_V = 10.9$) and the data set used is from a Huntsman camera (83F010774) that was defocused, collected on 18 September 2018 (see Table 3.1). The lower plot in Figure 4.2 is S/N_{diff} calculated for different aperture radii, where S/N_{diff} peaks at $r = 15$ pixels, and decreases abruptly towards the left and the right of this radius value. This peak has a corresponding small standard deviation in the upper plot of this same Figure, which is expected at the optimal aperture (see blue line in both plots).

The apertures used in the photometry of this same data set are shown in the left-hand panel of Figure 4.3. This image follows an effective PSF (ePSF) approach (Anderson & King, 2000). The ePSF is the net PSF of the observation and was built empirically from a stack of 50 images, to describe the amount of light in each of the pixels. The right-hand panel in Figure 4.3 is a horizontal cut of the

³For the computation of S/N_{diff} the readout noise is taken from Table 2.1

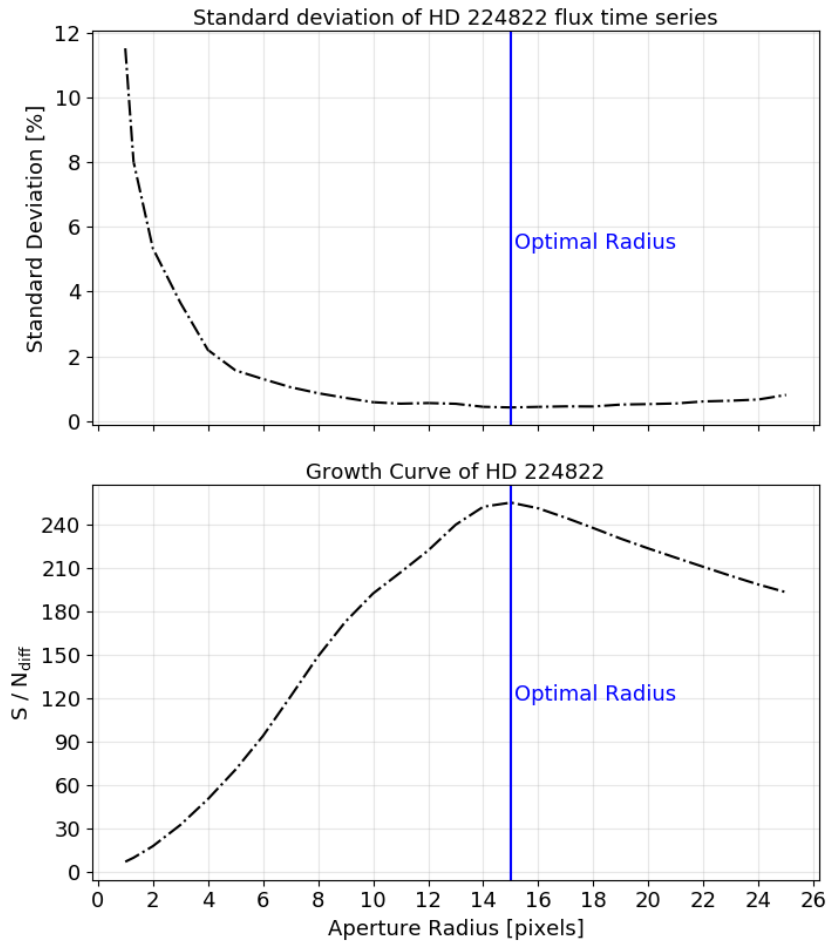


FIGURE 4.2: *Upper panel:* Standard deviation of a differential flux time series as a function of aperture radius. The aperture photometry to get the time series for each radius is performed, and then its standard deviation is computed. *Lower panel:* S/N_{diff} as a function of the aperture radius. This curve facilitates the analysis of the aperture size we should use in order to maximise the S/N_{diff} of an observation. Both panels use data that was collected with a defocused Huntsman camera on 18 September 2018.

ePSF on the left-hand panel. We can see that for this defocused camera the diameter⁴ of the optimal aperture was ~ 30 pixels, and the FWHM of the PSF was ~ 24 pixels; that is, the aperture contained most of the signal of the target star.

An in-focus camera (83F011167) has an optimal aperture radius that is considerably smaller (i.e. 4 pixels) than for a defocused camera, as shown in the lower plot of Figure 4.4. This results in a large standard deviation of the light curve as shown in the upper plot of the same Figure. For this in-focus camera the FWHM of the PSF is ~ 4 pixels (see the right-hand panel of Figure 4.5).

⁴For the sake of clarity, to compare the optimal aperture and the FWHM of the PSF we are using the aperture diameter instead of the radius.

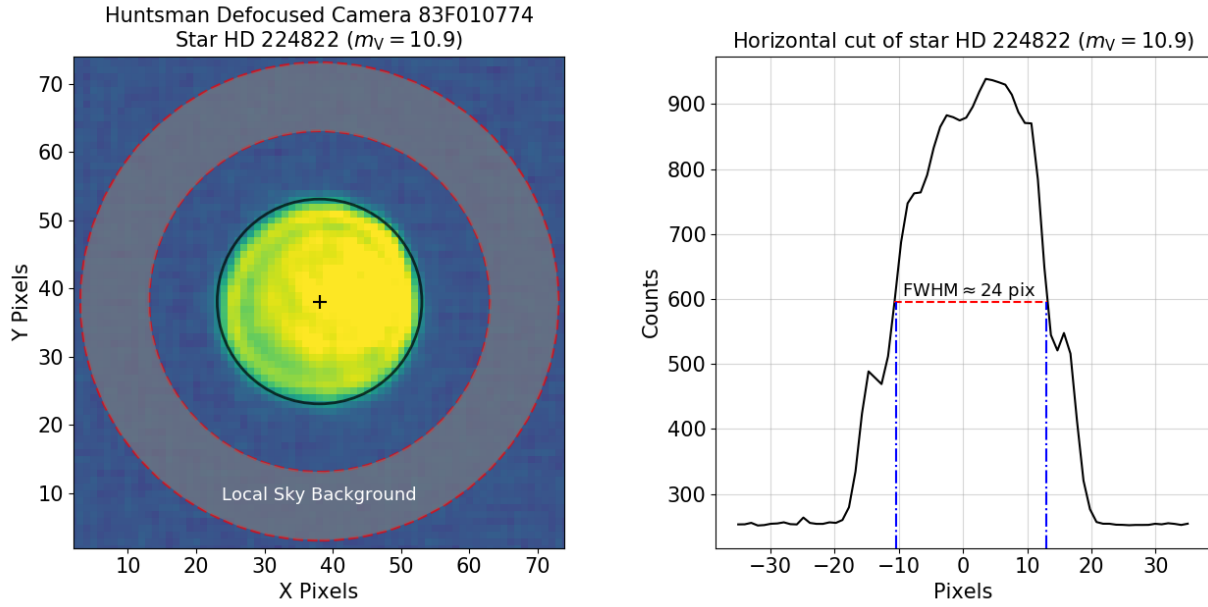


FIGURE 4.3: *Left-hand panel:* Circular aperture for the target star HD 224822 (blue inner circle) and annular aperture for the local background approximation (red annulus and grey shadow). All the circles are centred in the black cross marker which is obtained after finding the centroid using a two-dimensional Gaussian function `centroid_2dg` from `photutils`, included in the photometry pipeline of Huntsman. *Right-hand panel:* Horizontal cut from the sub-image in the left-hand panel made at the optimal aperture radius. The FWHM of the PSF is approximately 24 pixels, which is close to the diameter of the optimal aperture (i.e. ~ 30 pixels) in the left-hand panel

Therefore, for this in-focus camera the diameter of the optimal aperture is ~ 8 pixels, and approximately a factor of two larger than the FWHM of the PSF. This is different to the defocused case where both had similar sizes. With an in-focus camera we concentrate a large amount of light in few pixels (see the left-hand panel in Figure 4.5), and the wings of the stellar PSF contaminate more the background. At the same time, as the diameter of the optimal aperture is about twice the FWHM, this means that we are including more signal from the sky background within the aperture, which is detrimental to achieve high-precision photometry.

For both in-focus and out-of-focus scenarios, the optimal aperture maximises S/N_{diff} but excludes a significant amount of flux from the wings of the star too. A solution offered by Howell (1989), described as an azimuthal-averaged profile-fitting technique, relies on constructing growth curves to show how each source keeps growing with the aperture-size (where the flux is added up). With Huntsman, I found the right size of the aperture by assuming that the S/N_{diff} curve of a very bright target can be used as a guide for the whole frame. This includes those faint objects that are more prone to be affected because of an incorrect subtraction of the sky background, or even due to the presence of many stars too close from the target (i.e. in crowded fields).

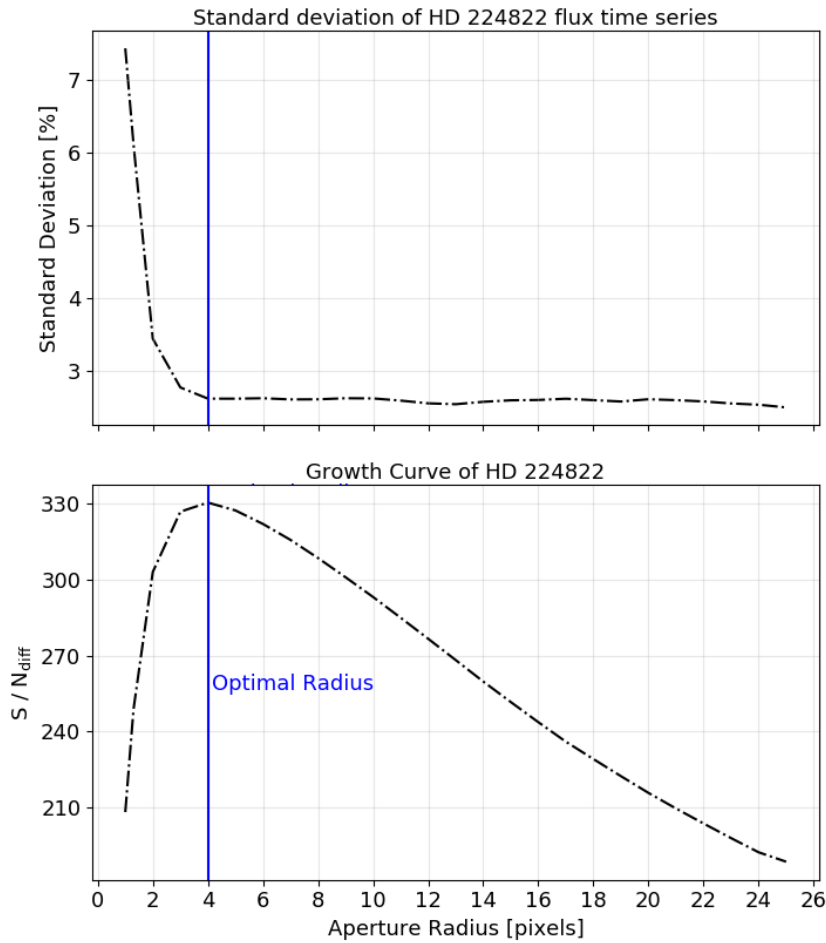


FIGURE 4.4: Same description of Figure 4.2, but this time using a Huntsman in-focus camera. As evident, the optimal radius is smaller than for a defocused camera since the starlight is more concentrated in fewer pixels.

To find the optimal aperture we must take into account the brightness of the target star. The PSF of a faint target is small, so a large aperture is not suitable to maximise S/N_{diff} . On the other hand, if the target is bright the PSF is larger, which requires the use of large apertures that contain most of the light. Therefore, in order to improve the photometric precision, the optimal aperture should be calculated individually for each star.

4.4 HUNtsman PHOtometry Pipeline (HUPHOP)

The photometry pipeline for derivation of transit light curves from Huntsman exoplanet data, was implemented as a critical part for the success of this thesis. HUPHOP v1.0 is a command-line based code

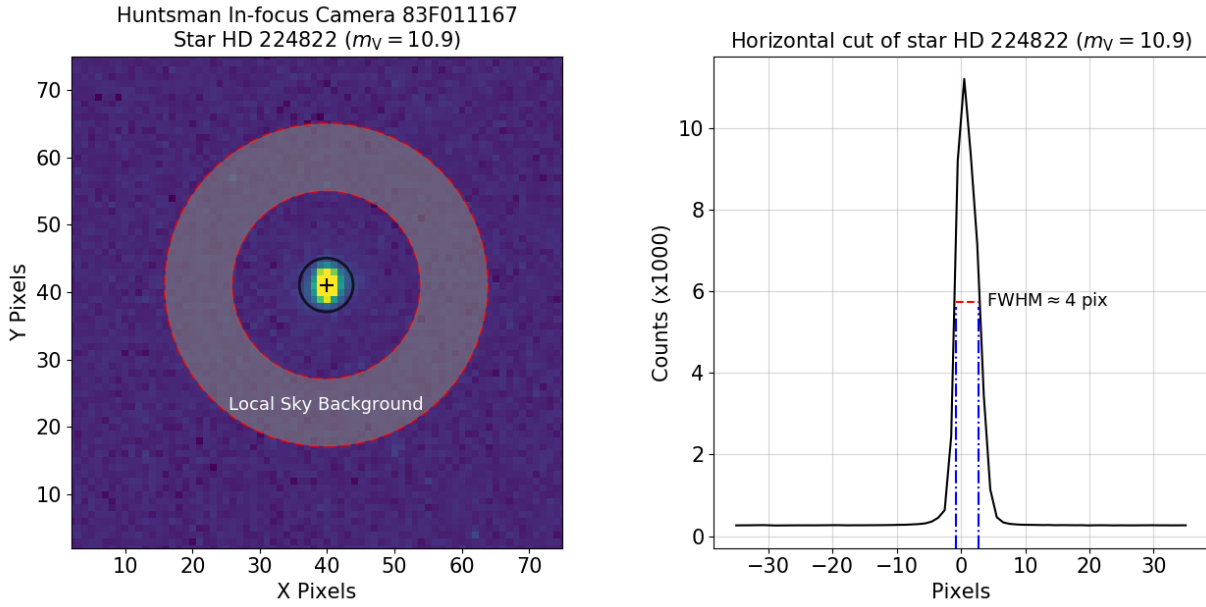


FIGURE 4.5: *Left-hand panel:* Same description of the left-hand panel in Figure 4.2, but for a Huntsman in-focus camera. *Right-hand panel:* Horizontal cut from the sub-image in the left-hand panel made at the optimal aperture. In this case the FWHM of the PSF (~ 4 pixels) is a factor of two smaller than the diameter of the optimal aperture (~ 8 pixels).

written in the programming language Python 3, making use of packages from [Astropy Collaboration et al. \(2013, 2018\)](#) (e.g. `ccdproc`, [Craig et al. 2015](#)), image processing functions from `photutils` ([Bradley et al., 2018](#)), and other Python-related packages like `pandas` ([McKinney, 2010](#)), `numpy` ([Oliphant, 2006](#)), and `matplotlib` ([Hunter, 2007](#)). HUPHOP is designed with the aim of being easily adaptable to any data set taken from any telescope, with only few parts that would need to be changed manually. This will be further improved in a future version of HUPHOP, along with other features that can also be optimised. HUPHOP makes use of plate-solved images provided directly by POCS, which undergo the data reduction process explained in [section 3.3](#). If the images are not plate-solved, HUPHOP has a built-in function to build the right ascension and declination for each star in a given image. The observed stars for this research are bright, and defocused photometry is the main strategy to reduce systematic errors, so PSF fitting is not an appropriate technique for the photometry analysis.

The user needs to provide HUPHOP with the name of the target star and reference stars, which can be adopted from any catalogue. The list can be composed of any number of stars. Once the user provides these names, HUPHOP finds automatically a *prior* coordinate pair for the centroid of each star using `Astropy`. A refined calculation of the centroids is then carried out in each science frame using the two-dimensional Gaussian function `centroid_2dg` from `photutils`, and employing a median filter to exclude most of the pixels with background signal, so that the final pixel coordinates for each

star centroid, $(x_{\text{cen}}, y_{\text{cen}})$, is found. This same centroid is then adopted for both the object aperture (circular) and the local background aperture (annular). The radii of these apertures are inputs of the pipeline that the user has to set in pixel units, and any user should follow the method explained in [section 4.3](#) to adopt optimal aperture radii in order to achieve the best photometric precision when using HUPHOP, and in general, this method should be followed for any aperture photometry software.

The next stage of HUPHOP is to perform the aperture photometry, where the user can select among three different methods for the apertures: `center`, `subpixel`, and `exact`. The `center` method includes any pixel whose centre is within the aperture, `subpixel` divides each pixel into $N \times N$ subpixels and applies the `center` method for each subpixel; and `exact` computes the exact fraction (a number from 0 to 1) of each pixel that is within the aperture. For the computing of all the light curves in this thesis, the `exact` method was selected, as it resulted in the best photometric precision.

HUPHOP was designed with a novel way of structure, namely, a Data Type Class called `DiPhot`. This is a Python class composed of different `function` objects that can be called altogether to perform the whole photometric analysis, or individually if we want to use them as `methods` for new instances of `DiPhot`. To do a light curve for a given data set, HUPHOP creates a new class instantiation operator (instance) called `photometry_analysis`, and invokes automatically the `__init__()` method for this newly-created instance of class `DiPhot` to parse all of the previously mentioned input parameters needed to perform the differential photometry.

4.5 Huntsman Light Curves

For high-precision analysis of any Huntsman data set, HUPHOP combines manual photometry with automated data-extraction techniques. To obtain the best photometric precision from our observational runs, it is paramount to have high-quality data to feed HUPHOP. As mentioned in [subsection 3.1.1](#), the observed targets were adequately bright to increase the signal and reduce common noise sources like photon noise, scintillation, sky-background contamination, etc. For the purpose of this thesis, only data with good telescope guiding was selected.

To make all light curves shown in this section, I have selected the observational run made on 18 September 2018 (see [Table 3.1](#)) for the target star HD 224822 ($m_V = 10.9$), and used a close group of four non-variable reference stars in the same field of view, without angular correlation with the target

star ⁵. The reference stars were⁶: TYC 8464-1282-1 ($m_V = 10.57$), HD 224582 ($m_V = 9.02$), CD-55 9417 ($m_V = 10.16$), and CD-55 9406 ($m_V = 10.68$). Two telescope focus modes were explored, and the current analysis starts from the results obtained when using in-focus photometry (Figure 4.6 and Figure 4.7), and ends with the optimal precision achieved via telescope defocusing, as shown later in Figure 4.8. The side-by-side comparison of in-focus and defocused photometry illustrates the importance of pixel-to-pixel effects, and highlights the potential of the Huntsman telescope.

The formalism of Southworth et al. (2009a) was adopted to compute the amplitude error of all different noise sources in the light curves of this section. Using equations (4.2), (4.3), and (4.4) we can find the relative amplitude errors of photon, sky-background, and readout noise, respectively. These are compared to the total electrons from the target star in magnitude (or relative flux) units as follows,

$$\sigma_{\text{phot}} = -2.5 \log_{10} \left(\frac{S_{\text{phot}} - N_{\text{phot}}}{S_{\text{phot}}} \right), \quad (4.10)$$

$$\sigma_{\text{sky}} = -2.5 \log_{10} \left(\frac{S_{\text{phot}} - N_{\text{sky}}}{S_{\text{phot}}} \right), \quad (4.11)$$

$$\sigma_{\text{read}} = -2.5 \log_{10} \left(\frac{S_{\text{phot}} - N_{\text{read}}}{S_{\text{phot}}} \right). \quad (4.12)$$

Therefore, to compute the total photometric error in one observation, we have four noise sources that can be added in quadrature, namely, scintillation (Equation 1.1), photon noise (Equation 4.10), sky-background noise (Equation 4.11), and readout noise (Equation 4.12):

$$\sigma_{\text{total}} = \sqrt{\sigma_{\text{phot}}^2 + \sigma_{\text{sky}}^2 + \sigma_{\text{scint}}^2 + \sigma_{\text{read}}^2}. \quad (4.13)$$

Figure 4.6 shows the time series photometry for the Huntsman in-focus cameras 83F010801, 83F011167, and 83F011791, where each light curve was made using the optimal radius given by the S/N_{diff} curve of each camera (see e.g. Figure 4.4 for 83F011167). The precision achieved in each of them is different, being the highest precision that of the 83F010801 with a standard deviation of 2.61%. For the star HD 224822 ($m_V = 10.9$) the optimal radius of the stellar PSF was 4 pixels in all three in-focus cameras, and 14/24 pixels for the inner/outer radii of the sky annulus respectively. So, the PSF aperture covered approximately 50 pixels and the sky annulus covered 1194 pixels.

⁵The degree at which stars are correlated is dependent on the angular separation of all stars from each other, and 20" is the typical radius for correlation (Kornilov, 2012).

⁶The information for each star was extracted from <http://simbad.u-strasbg.fr/simbad/>

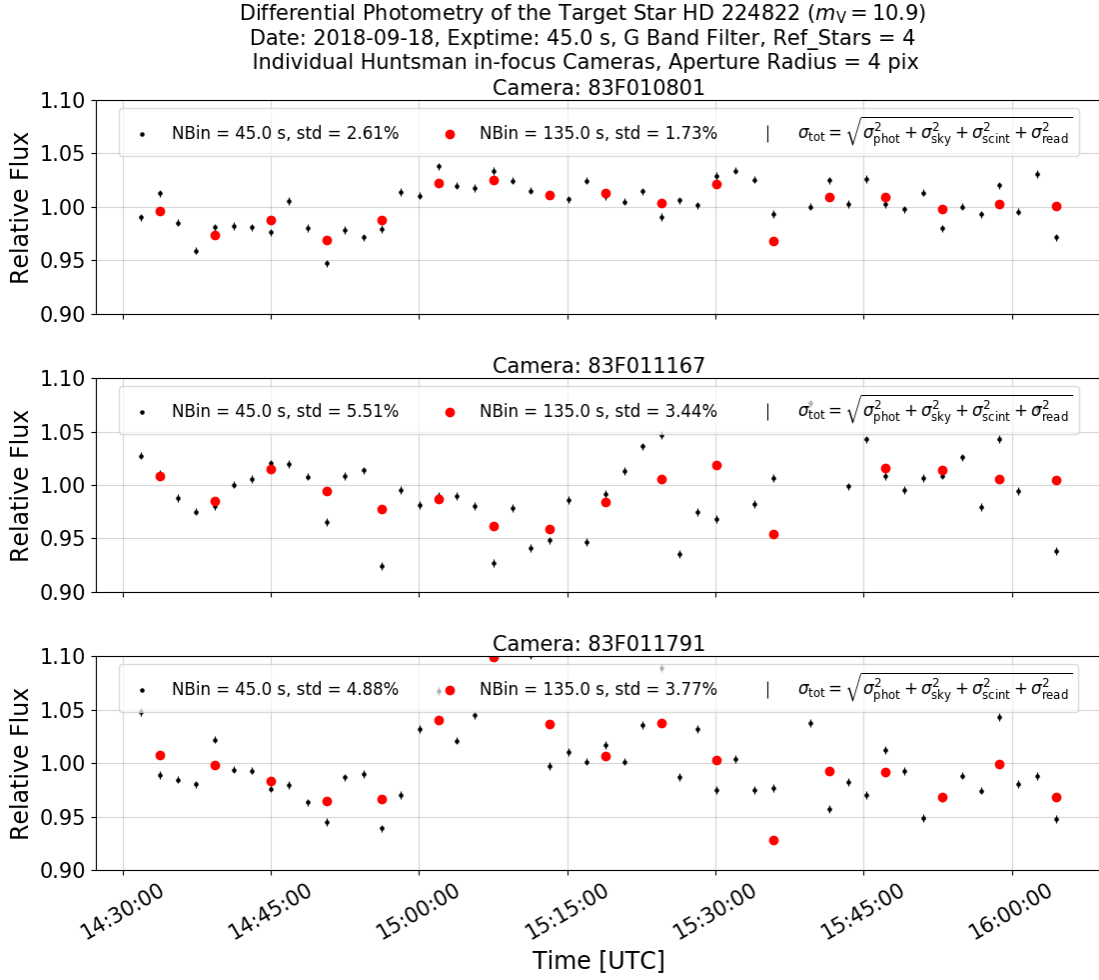


FIGURE 4.6: Flux time series of the target star HD 224822, using Huntsman cameras 83F010801 (upper panel), 83F011167 (middle panel), and 83F011791 (lower panel). The optimal radius is 4 pixels for all the three in-focus cameras. Both the unbinned (45 s) and binned (135 s) data are plotted in black and red, respectively. The data set of this plot was collected on 18 September 2018, using a G band filter.

The total amplitude error (the error bars shown) is given by Equation 4.13, which for the in-focus cameras of Figure 4.6 is considerably smaller, unlike the standard deviation of the light curves. No sigma-clipping was used so all frames were taken into account to compute the standard deviation. We can see in Figure 4.6 that even for binned data (red dots) the time series has a significantly high scatter, and while it reduces for the binned data, the dispersion is still quite large for exoplanet photometry. The binning was done every three frames, for a window of 135 s. These light curves for in-focus cameras present noise that is not Gaussian, possibly due to systematic errors in the tracking of the mount and pixel-to-pixel sensitivity variations of the ubiquitous CCDs, which were not characterised within the purpose of this thesis and left for future research of my PhD.

One of the main objectives of this thesis is to test whether the use of multiple small apertures can improve the overall photometric precision by increasing the effective aperture of the instrument.

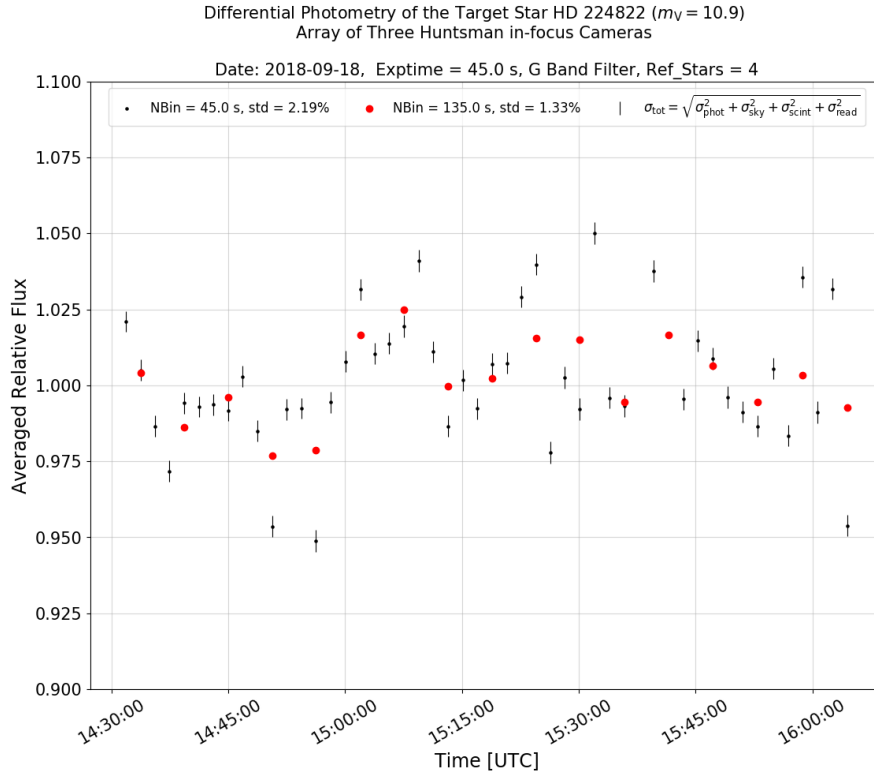


FIGURE 4.7: Averaged flux time series of the target star HD 224822 for three Huntsman in-focus cameras: 83F010801, 83F011167, and 83F011791. We achieved a standard deviation of 1.33% when binning in intervals of 135 s. It is worth noticing that the photometry precision improves with respect to the individual cameras (see Figure 4.6). The data set of this plot was collected on 18 September 2018, using a G band filter.

To investigate this point, an integrated light curve was produced, where the fluxes of the previous three in-focus cameras were averaged. In Figure 4.7 is shown the averaged relative flux from cameras 83F010801, 83F011167, and 83F011791. For the computing of the standard deviation of this plot three outliers were clipped, which were located 3 sigma values beyond the mean of the distribution. For this process I used the function `sigma_clip` from the package `astropy.stats` of Astropy Collaboration et al. (2013, 2018).

For both the unbinned and binned data, the resulting standard deviation of the light curve in Figure 4.7 is lower than the three light curves of the in-focus cameras in Figure 4.6. This result indicates that using multiple small apertures is an effective way to improve the photometric precision. However, the resulting standard deviation is still too large to capture a planetary transit (i.e. 2.19%, see Figure 4.7). I will further explore this during my PhD, once Huntsman is ready to work with the full array of ten lenses, and using telescope defocusing in all cameras, as explained below.

Figure 4.8 shows defocused imaging analysis from camera 83F010774 on the 18th September 2018 for the target star HD 224822 (see the left-hand panel in Figure 4.3), and with the same vertical

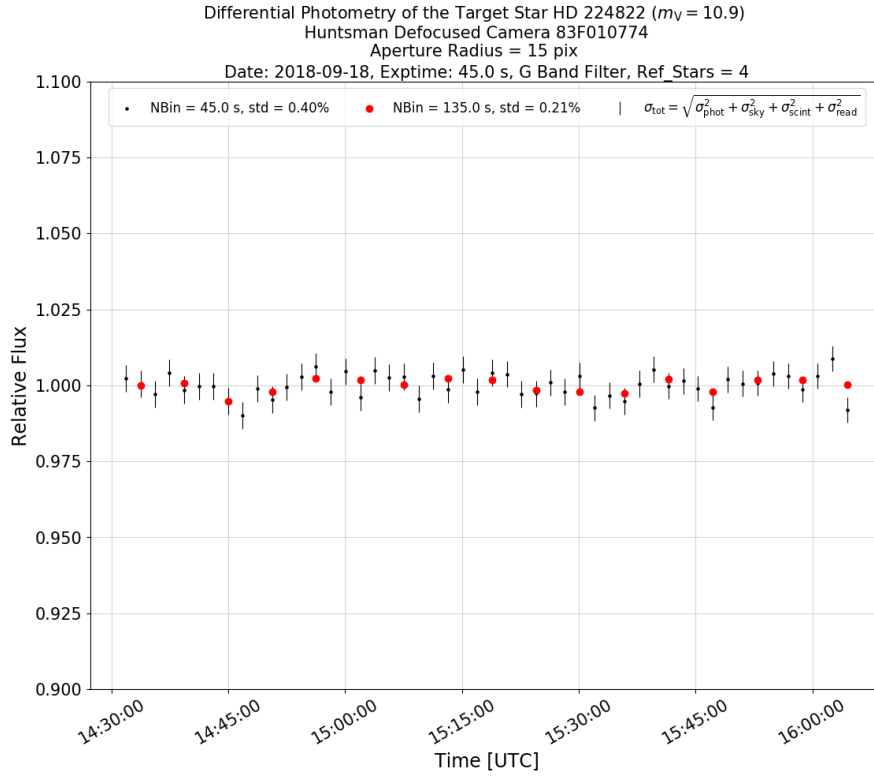


FIGURE 4.8: Flux time series of the target star HD 224822, using telescope defocusing in Huntsman camera 83F010774. The optimal radius is 15 pixels and is extracted from Figure 4.2. Both the unbinned (45 s) and binned (135 s) data are plotted in black and red, respectively. The data set of this plot was collected on 18 September 2018, using a G band filter. The precision achieved in the binned data set is 0.21%.

scaling of Figure 4.7. The optimal aperture radius for the PSF of the star (~ 15 pixels) is given by the S/N_{diff} in Figure 4.2, and 25/35 pixels for the inner/outer radii of the sky annulus, respectively. Thus, the PSF aperture covered approximately 1000 pixels and the sky annulus covered 1885 pixels.

The precision for the defocused camera is one order of magnitude better than for each of the three in-focus cameras, for both the unbinned and binned data. To compute the standard deviation, again no value was discarded, and all 50 frames were used. We can notice that when using telescope defocusing the scattering of the light curve is very similar to the predicted total noise given by equation Equation 4.13 (error bars shown in Figure 4.8), and extremely low as opposed to in-focus photometry. The evolution of the noise sources for the light curve in Figure 4.8 are shown in Figure 4.9. We can see that during most of the night the major contribution is that of the photon noise (dark red), followed by the sky background (blue), readout noise (red), and scintillation (green) in last place. All of them have a significant contribution to the total noise represented by the black line in the same Figure.

The photometric precision of 0.4% in Figure 4.8 would allow us to observe transits of Jupiter-like planets, which is the majority of currently known exoplanets (see Chapter 1). Therefore, except for very

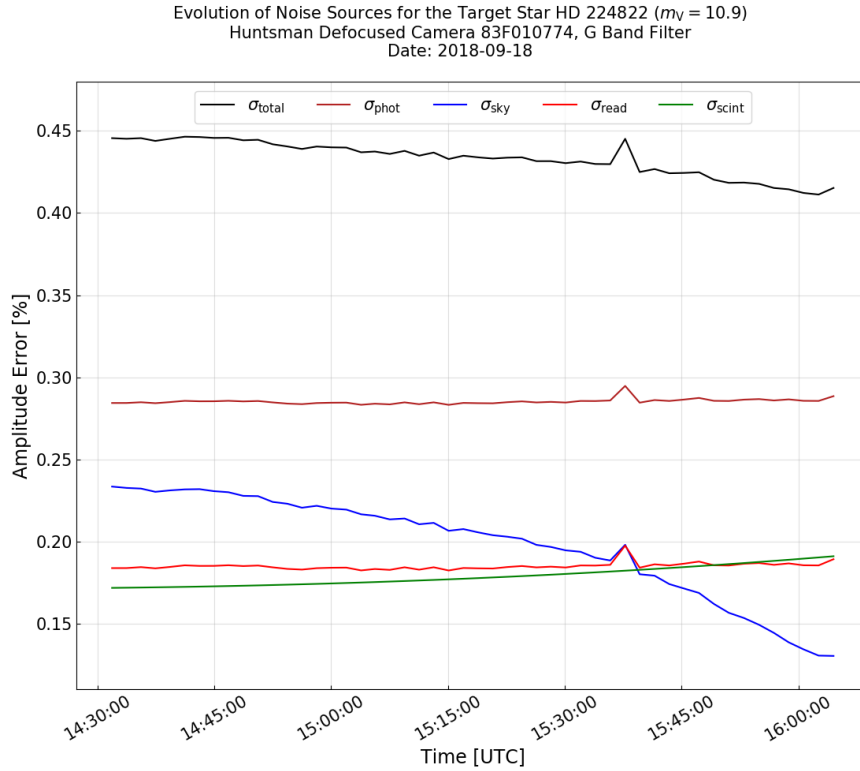


FIGURE 4.9: Evolution of noise sources in the target star HD 224822 during the observational run on 18 September 2018. The bump observed at $\sim 15:40:00$ (UTC) was probably caused by a transparency variation. The major contribution to the total noise comes from photon noise, followed by sky background which decreased until readout noise became more dominant. Scintillation noise increased with the airmass of the target star towards the right-hand side of the plot.

faint targets, telescope defocusing is clearly the preferred approach for doing exoplanet photometry with the Huntsman Telescope. Some ground-based studies have used telescope defocusing to improve significantly the photometric precision of light curves like for HD 189733b (Winn et al., 2007a), HAT-P-1b (Winn et al., 2007b), WASP-5b (Southworth et al., 2009a), WASP-4b (Southworth et al., 2009b), GJ 436 b (Demory et al., 2007, Alonso et al., 2008), and HD 17156b (Gillon et al., 2008).

It is worth noticing that there is still room for improvement – the defocusing has not yet been optimised for Huntsman, so potentially a better precision can be achieved. Indeed, one can maximise the precision by equally distributing the signal of the target (S_{target}) over a number of pixels $n_{\text{def,pix}}$ according to the method of Southworth et al. (2009a):

$$n_{\text{def,pix}} = \frac{S_{\text{target}}}{m_{\text{total}} - R_{\text{sky}} G t_{\text{exp}}}, \quad (4.14)$$

where m_{total} is the number of electrons we want in each pixel coming both from the target and the background, t_{exp} the exposure time, and R_{sky} the number of ADUs per second per pixel from the sky background. This has to be balanced against background blends, and exposure times considerations.

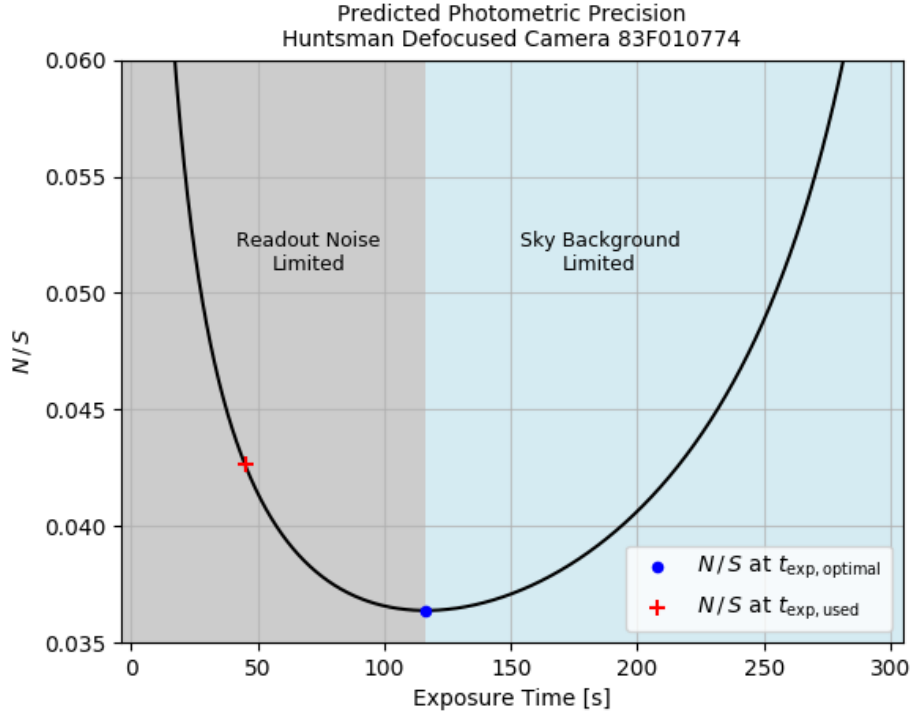


FIGURE 4.10: Theoretical noise-to-signal ratio per unit time as a function of the exposure time. The blue dot represents the optimal exposure time (i.e. 116 s) we should have used with the Huntsman defocused camera 83F010774 on the night of the 18th September 2018. The optimal integration time is intermediate for observations that are not readout noise limited (grey region) or sky background limited (light blue region).

The exposure times for a given defocusing of the telescope change according to the predicted level noises, which in this case are photon (Equation 4.10), sky-background (Equation 4.11), and scintillation (Equation 1.1). Readout noise is excluded in this analysis because it is independent of the exposure time, and instead depends on the number of pixels within the aperture. With this in mind, for short exposures we would be limited by CCD readout, whereas for long exposures the sky-background dominates. In order to illustrate such regimes, we can compute the noise-to-signal ratio per unit time as explained by Southworth et al. (2009a),

$$N/S = \sigma_{\text{total}} \sqrt{t_{\text{exp}} + t_{\text{dead}}}, \quad (4.15)$$

where σ_{total} is the total photometric error given by Equation 4.13, and t_{dead} is the total dead time between consecutive exposures. Equation 4.15 is plotted in Figure 4.10, where we can find the exposure time used for the defocusing of this thesis (45 s, red cross), and the optimal exposure time that we should have used for such a defocusing (116 s, blue dot). I plan to implement at a future date the computation of the optimal amount of defocusing and exposure time, as automated tasks of Huntsman’s control system (i.e. POCS, see subsection 3.1.1).

Summary and Discussion

The Huntsman Telescope, funded by Macquarie University, is operated by a team of professional astronomers and instrumental scientists. Huntsman consists of an assembly of telephoto lenses pointed at the same target, increasing the effective aperture of the instrument and improving its photometric precision. This thesis is the first step in an effort to use Huntsman in the discovery and follow-up observation of exoplanets. Despite commissioning issues which still need to be resolved, I was able to demonstrate that Huntsman is suitable to perform high-precision observation of bright stars.

Follow-up observations of exoplanet candidates found by space-based missions requires a large number of ground-based telescopes. The Huntsman Telescope is a type of small facility that can be deployed quickly due to the off-the-shelf availability of its components. In addition, when compared to other similar facilities like SuperWASP, Huntsman is a cost-effective telescope that can reach the same, or even better performance than facilities specifically designed for exoplanet work.

This thesis shows that we can achieve high-precision photometry with Huntsman at the 0.5% level or better. I obtained this result from the optimisation of all parts involved in photometry, and derived the optimal strategy for observing bright transit targets. The Huntsman Telescope is designed to have a stable PSF, low scattered light and close to zero ghosts, no central obstruction, and suitable aperture; and I have shown that all of these characteristics combine to make Huntsman a precision photometry tool for efficient exoplanet follow-up.

The most important experiment I did for this thesis was using four active Huntsman cameras in the same night, which enabled a side-by-side comparison of the achievable precision via in-focus and defocused photometry. The advantages of defocused photometry are having larger PSFs (low flat-fielding errors), longer exposure times, which means less time spent reading out the CCD; more photons per frame, and less scintillation noise. The drawbacks of this technique include a lower time resolution of light curves, which can be improved using the method mentioned at the end of

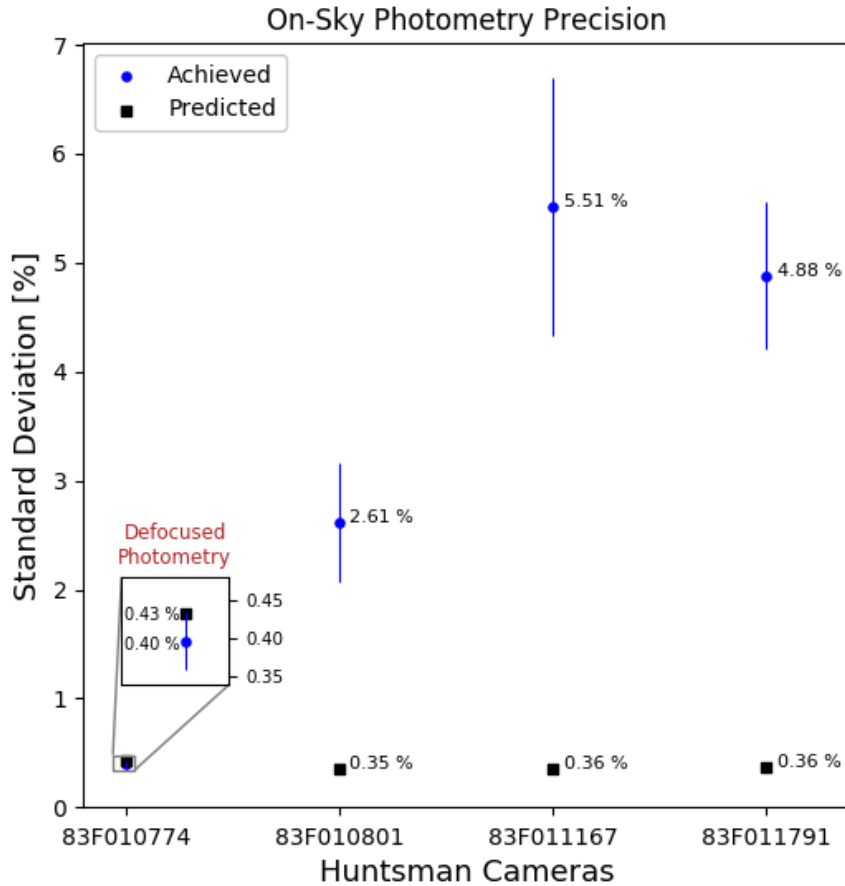


FIGURE 5.1: Photometry precision for one defocused (83F010774, see Figure 4.8) and three in-focus (83F011167, 83F010801, and 83F011791 see Figure 4.6) Huntsman cameras. The predicted standard deviation given by photon noise (Eq. 4.10), sky background noise (Eq. 4.11), scintillation (Eq. 1.1) and readout noise (Eq. 4.12) is plotted in black colour (squares) and the achieved photometric precision of the flux time series is plotted in blue colour (dots). Again, we can see that the best on-sky precision corresponds to the camera where telescope defocusing was used. The precision shown on this plot is for the unbinned data (45 s) of the light curves in section 4.5. The precision of the binned data (i.e. for a window of 135 s) reached $\sim 0.2\%$ for the camera 83F010774 (not shown on this plot).

section 4.5; a higher probability of contamination by blends with other stars, and higher background than in-focus photometry (unimportant for bright stars).

I demonstrated that by using telescope defocusing, high-precision photometry can be achieved with Huntsman – the predicted standard deviation was 0.43%, perfectly matching the $\sim 0.4\%$ that I actually achieved in the unbinned data (see camera 83F010774 Figure 5.1). In-focus photometry, however, failed to obtain good photometric precisions (see cameras 83F010801, 83F011167, and 83F011791 in Figure 5.1). Planetary transits produce variations in the stellar flux from 0.01% (Earth-like) to 1% (Jupiter-like), which means that light curves with high standard deviations are useless for detecting any

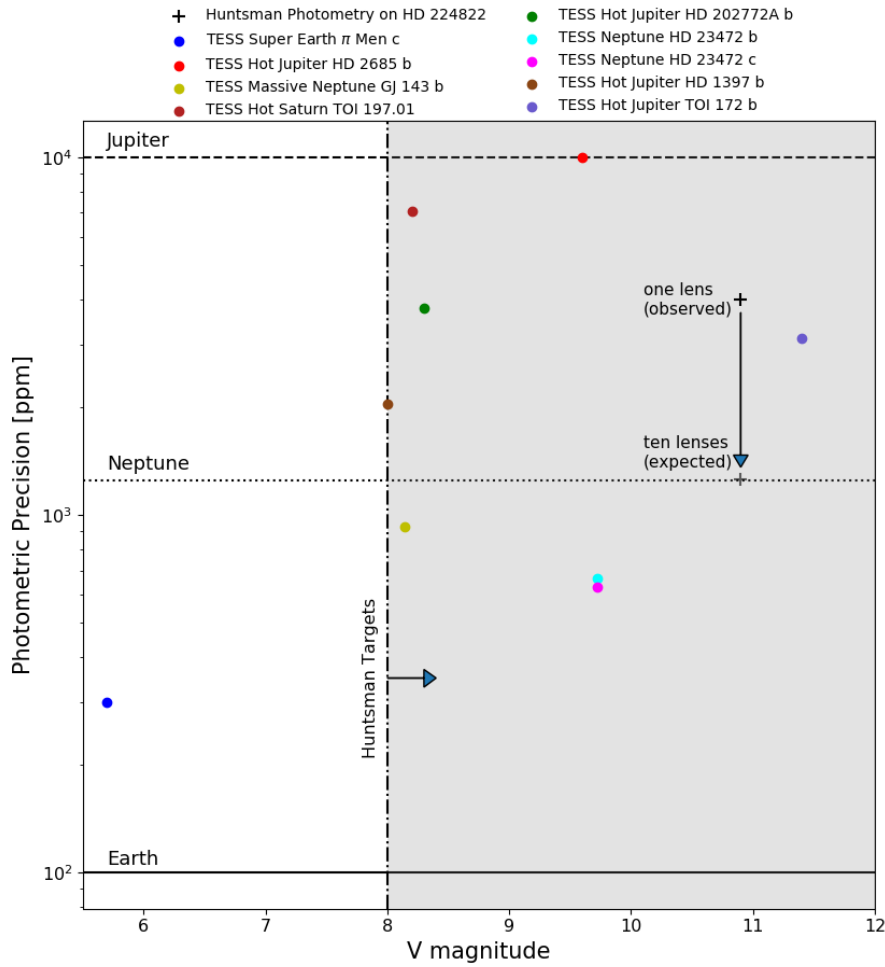


FIGURE 5.2: This plot contains the precisions needed to detect any transit of the confirmed TESS planets (refereed) to date. Three different regimes are shown, namely, Jupiter-like, Neptune-like, and Earth-like planets (dashed, dotted, and solid horizontal lines respectively). The dashed-dotted vertical line stands for the target stars I aim at observing with Huntsman. The precision I found in this thesis when using one camera system for the target star HD 224822 is shown as a black cross. The expected precision for the future Huntsman array (10 lenses) is also shown. All TESS exoplanet discoveries with their corresponding publication can be found at <https://heasarc.gsfc.nasa.gov/docs/tess/tpub-exoplanets.html>

exoplanet. Huntsman’s photometric precision when using defocused photometry allows us to observe Jupiter-like planets, and by binning over multiple exposures, and across the future array of Huntsman lenses, measuring the signal produced by Neptune-like planets will be possible.

I show in Figure 5.2 all the TESS confirmed planets to date: π Men c (Huang et al., 2018), HD 2685 b (Jones et al., 2018), HD 202772A b (Wang et al., 2019), HD 23472 b (Trifonov et al., 2019), HD 23472 c (Trifonov et al., 2019), GJ 143 b (Trifonov et al., 2019), TOI 197.01 (Huber et al., 2019), HD 1397 b (Nielsen et al., 2019), and TOI 172 b (Rodriguez et al., 2019). The precision I found with Huntsman using telescope defocusing on the bright star HD 224822 is depicted in Figure 5.1, employing only one camera (black cross marker). The expected precision of ten lenses is also depicted.

Finally, a significant product of this thesis was the design of an efficient software photometry pipeline, which can quickly turn future exoplanet data sets into useful light curves. Indeed, the future goal is to enable the confirmation of future TESS exoplanet candidates for Huntsman and other facilities. Once the Huntsman 10-lenses array is operating, it will work automatically and observe a significant number of exoplanet host stars. Therefore, given the short time-scales of exoplanet detection, I have also begun to build the necessary software to handle, reduce, and analyse all the upcoming data. The clear need for the Huntsman Telescope is expanding defocused photometry to all the lenses. This will increase the achievable photometric precision of Huntsman, and by combining data from all cameras we can reduce systematic errors.

5.1 Future Work

The Huntsman team has applied for observing time on the red-sensitive high-resolution Veloce spectrograph (Gilbert et al., 2018). Veloce is designed for the observation of M-dwarfs with its red-sensitive spectral grasp, and will be used predominantly for TESS follow-up and observing cool stars with close-in habitable zones and short orbital periods. These exoplanet orbits have large velocity amplitudes that will enhance their detectability. Our team has full control over the Huntsman time and access, and I plan to observe the TESS targets during their predicted transits concurrently with Veloce. Photometric observations together with Radial Velocity measurements are an important tool to disentangle stellar noise from true RV signals, and with the combined measurements of both methods we can then determine the density of the observed exoplanets. I am guaranteed to have significant amounts of observing time with Huntsman to make abundant explorations in search of exoplanets, adding to the knowledge of exoplanets in our galactic neighbourhood. I will entirely dedicate my PhD to this work.

The discovery and follow-up observation of exoplanets is an exciting field of science. In the future, the proximity of TESS planets will allow astronomers to take advantage of the James Webb Space Telescope, for accurate inspection of their atmospheres using transit/eclipse spectroscopy (Cowan et al., 2015, Batalha et al., 2017, Benneke et al., 2017). The Huntsman Telescope is a valuable facility that will help us to contribute towards the confirmation of exoplanet candidates that are being detected by TESS. Once these planets are confirmed, we will understand more about the planetary formation, evolution, and final fate of exoplanetary systems around different types of stars, including those ones similar to our Sun.

Appendix

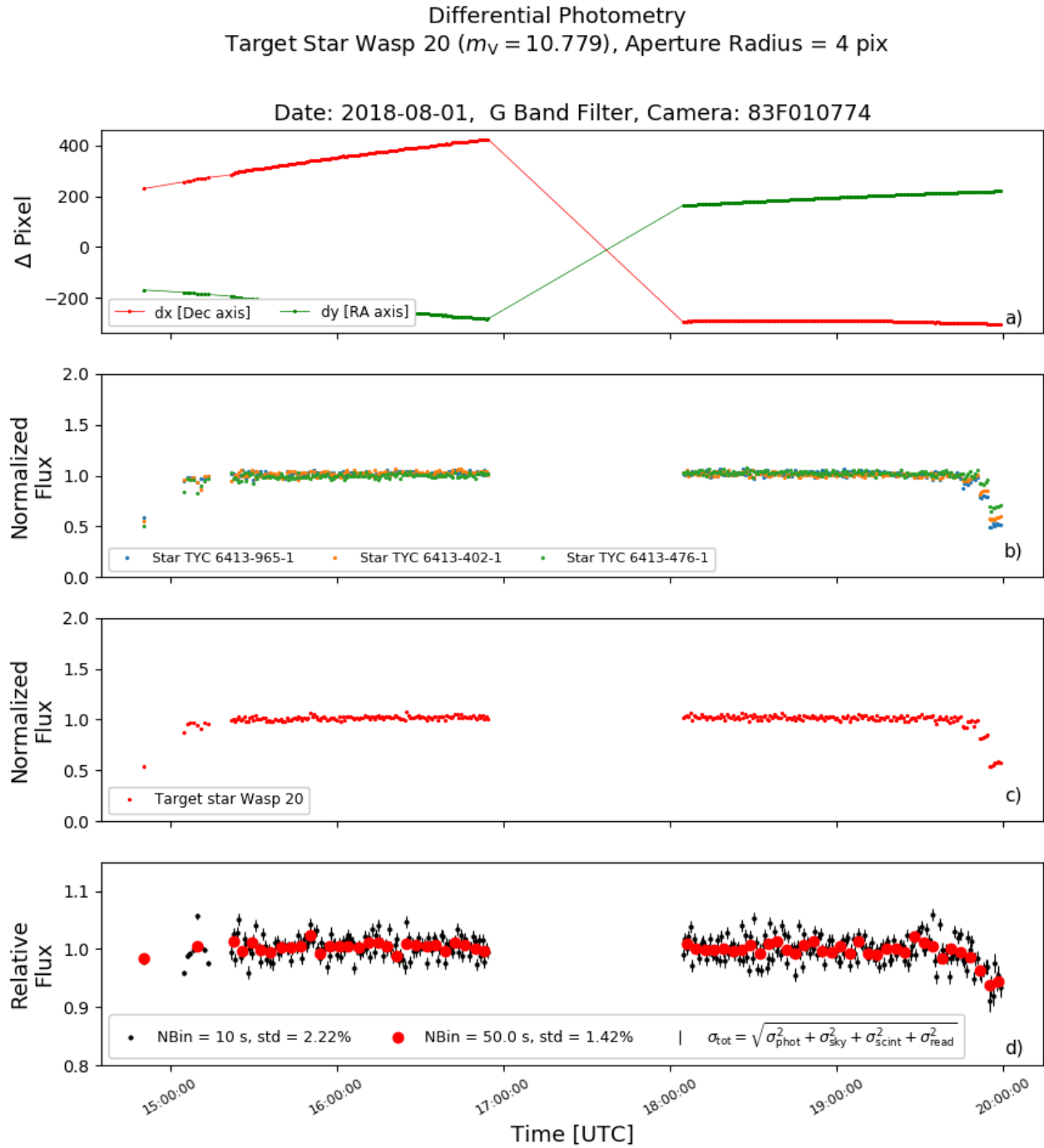


FIGURE A.1: Unexceptional Telescope Tracking. *Panel a)*: Variation of the target star's centroid position for both the right ascension (green line) and declination (red line) axes. The aperture radius is set to 4 pixels. *Panel b)*: Normalised flux for each of the reference stars. *Panel c)*: Normalised flux of the target star (i.e. aperture photometry of Wasp 20). *Panel d)*: Differential flux of the target star Wasp 20 respect to the integrated flux of the ensemble of reference stars. Both the binned (red dots) and the unbinned data (black dots) were plotted. The error bars correspond to the amplitude error caused by photon, sky background, scintillation, and readout noise. The data set of this plot was collected on 1 August 2018, using an exposure time of 10 s. This plot contains the data of a single Huntsman camera (83F010774).

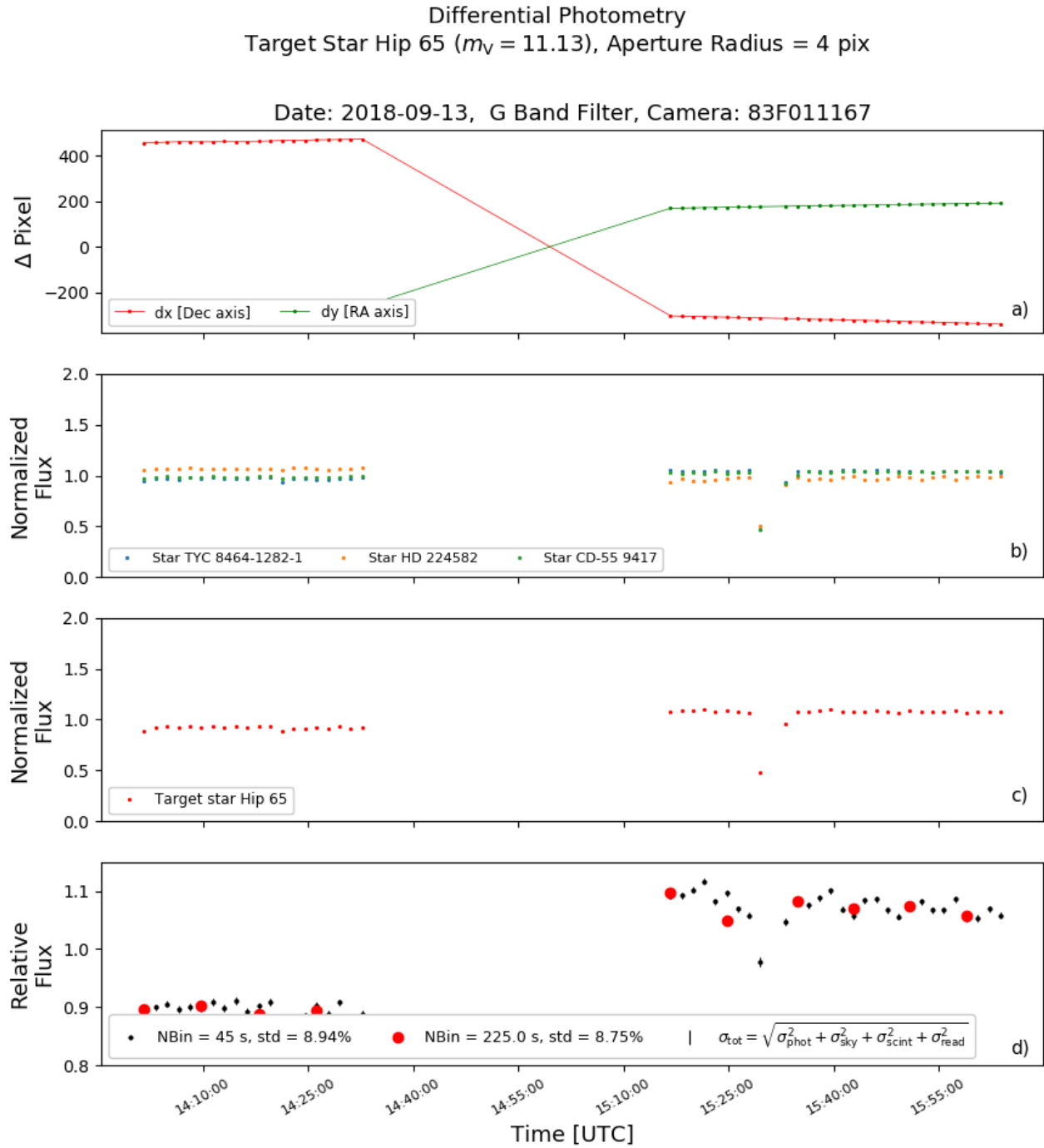


FIGURE A.2: Unexceptional Telescope Tracking. *Panel a)*: Variation of the target star's centroid position for both the right ascension (green line) and declination (red line) axes. The aperture radius is set to 4 pixels. *Panel b)*: Normalised flux for each of the reference stars. *Panel c)*: Normalised flux of the target star (i.e. aperture photometry of Hip 65). *Panel d)*: Differential flux of the target star HIP 65 respect to the integrated flux of the ensemble of reference stars. Both the binned (red dots) and the unbinned data (black dots) were plotted. The error bars correspond to the amplitude error caused by photon, sky background, scintillation, and readout noise. The data set of this plot was collected on 13 September 2018, using an exposure time of 45 s. This plot contains the data of a single Huntsman camera (83F011167).

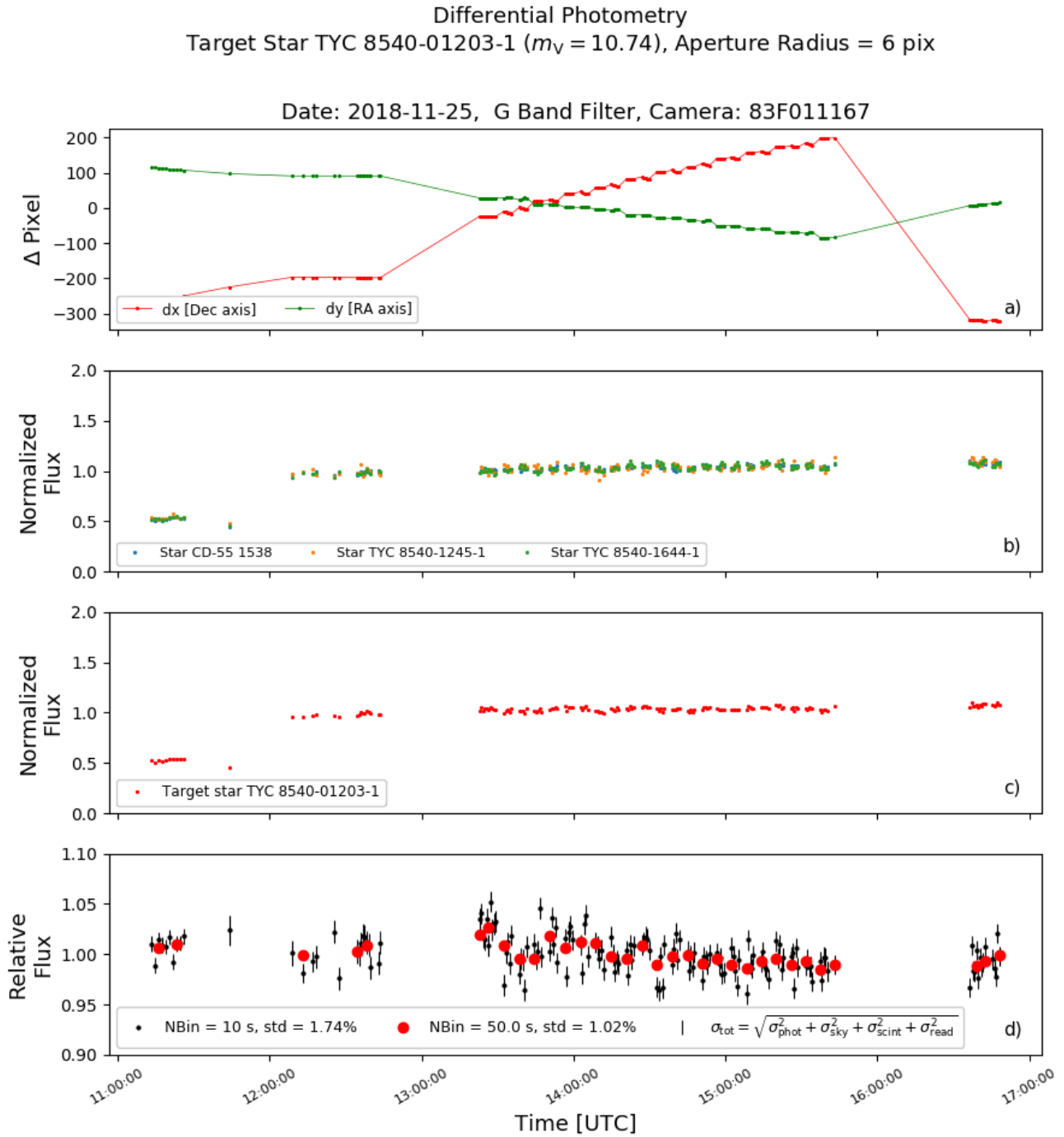


FIGURE A.3: Unexceptional Telescope Tracking. *Panel a)*: Variation of the target star's centroid position for both the right ascension (green line) and declination (red line) axes. The aperture radius is set to 6 pixels. *Panel b)*: Normalised flux for each of the reference stars. *Panel c)*: Normalised flux of the target star (i.e. aperture photometry of TYC 8540-01203-1). *Panel d)*: Differential flux of the target star TYC 8540-01203-1 respect to the integrated flux of the ensemble of reference stars. Both the binned (red dots) and the unbinned data (black dots) were plotted. The error bars correspond to the amplitude error caused by photon, sky background, scintillation, and readout noise. The data set of this plot was collected on 26 November 2018, using an exposure time of 10 s. This plot contains the data of a single Huntsman camera (83F011167).

References

- Alonso R., Barbieri M., Rabus M., Deeg H. J., Belmonte J. A., Almenara J. M., 2008, [A&A](#), **487**, L5
- Anderson J., King I. R., 2000, [PASP](#), **112**, 1360
- Anglada-Escudé G., et al., 2016, [nature](#), **536**, 437
- Astropy Collaboration et al., 2013, [A&A](#), **558**, A33
- Astropy Collaboration et al., 2018, [AJ](#), **156**, 123
- Auvergne M., et al., 2009, [A&A](#), **506**, 411
- Bakos G. Á., Lázár J., Papp I., Sári P., Green E. M., 2002, [PASP](#), **114**, 974
- Bakos G. Á., et al., 2013, [PASP](#), **125**, 154
- Baliunas S. L., Henry G. W., Donahue R. A., Fekel F. C., Soon W. H., 1997, [ApJL](#), **474**, L119
- Barclay T., Pepper J., Quintana E. V., 2018, [The Astrophysical Journal Supplement Series](#), **239**, 2
- Batalha N. E., Kempton E. M.-R., Mbarek R., 2017, [ApJL](#), **836**, L5
- Beck T., et al., 2017. , [doi:10.1117/12.2296216](#), [https://doi.org/10.1117/12.2296216](#)
- Benneke B., et al., 2017, [ApJ](#), **834**, 187
- Bertin E., Arnouts S., 1996, [A&A](#), **117**, 393
- Bessell M. S., 1990, [PASP](#), **102**, 1181
- Borucki W. J., Summers A. L., 1984, [icarus](#), **58**, 121
- Borucki W. J., et al., 2010, [Science](#), **327**, 977
- Boyajian T. S., et al., 2016, [MNRAS](#), **457**, 3988
- Bradley L., et al., 2018, astropy/photutils: v0.5, [doi:10.5281/zenodo.1340699](#), [https://doi.org/10.5281/zenodo.1340699](#)
- Burke C. J., et al., 2015, [ApJ](#), **809**, 8
- Charbonneau D., Brown T. M., Latham D. W., Mayor M., 2000, [ApJL](#), **529**, L45
- Christian D. J., et al., 2006, [MNRAS](#), **372**, 1117
- Collins K. A., Kielkopf J. F., Stassun K. G., Hessman F. V., 2017, [AJ](#), **153**, 77
- Colón K. D., Ford E. B., Redfield S., Fortney J. J., Shabram M., Deeg H. J., Mahadevan S., 2012, [MNRAS](#), **419**, 2233
- Cowan N. B., et al., 2015, [PASP](#), **127**, 311
- Craig M. W., et al., 2015, ccdproc: CCD data reduction software, Astrophysics Source Code Library (ascl:1510.007)
- Croll B., Lafreniere D., Albert L., Jayawardhana R., Fortney J. J., Murray N., 2011, [AJ](#), **141**, 30

- Crossfield I. J. M., et al., 2015, [ApJ](#), **804**, 10
- Da Costa G. S., 1992, in Howell S. B., ed., *Astronomical Society of the Pacific Conference Series Vol. 23, Astronomical CCD Observing and Reduction Techniques*. p. 90
- Dawson R. I., Johnson J. A., 2018, [Annual Review of Astronomy and Astrophysics](#), **56**, 175
- Deeg H. J., 2013, VAPHOT: Precision differential aperture photometry package, *Astrophysics Source Code Library* (ascl:1309.002)
- Demory B. O., et al., 2007, [A&A](#), **475**, 1125
- Dravins D., Lindegren L., Mezey E., Young A. T., 1998, [PASP](#), **110**, 610
- Fukugita M., Ichikawa T., Gunn J. E., Doi M., Shimasaku K., Schneider D. P., 1996, [AJ](#), **111**, 1748
- Fukui A., et al., 2016, [ApJ](#), **819**, 27
- Gee W. T., Guyon O., Walawender J., Jovanovic N., Boucher L., 2016, Project PANOPTES: a citizen-scientist exoplanet transit survey using commercial digital cameras, [doi:10.1117/12.2234461](#), [http://hdl.handle.net/10150/622806](#)
- Gilbert J., et al., 2018, preprint, ([arXiv:1807.01938](#))
- Gilliland R. L., et al., 1993, [AJ](#), **106**, 2441
- Gillon M., Triaud A. H. M. J., Mayor M., Queloz D., Udry S., North P., 2008, [A&A](#), **485**, 871
- Henry G. W., 1999, [PASP](#), **111**, 845
- Henry G. W., Baliunas S. L., Donahue R. A., Soon W. H., Saar S. H., 1997, [ApJ](#), **474**, 503
- Henry G. W., Marcy G. W., Butler R. P., Vogt S. S., 2000, [ApJL](#), **529**, L41
- Hidas M. G., et al., 2005, [MNRAS](#), **360**, 703
- Holwerda B. W., 2005, *ArXiv Astrophysics e-prints*,
- Howell S. B., 1989, [PASP](#), **101**, 616
- Huang C. X., et al., 2018, [ApJL](#), **868**, L39
- Huber D., et al., 2019, Accepted for publication in *AJ*, [p. arXiv:1901.01643](#)
- Hunter J. D., 2007, [Computing In Science & Engineering](#), **9**, 90
- Ikoma M., Nakazawa K., Emori H., 2000, [ApJ](#), **537**, 1013
- Irwin J., Charbonneau D., Nutzman P., Falco E., 2009, in Pont F., Sasselov D., Holman M. J., eds, *IAU Symposium Vol. 253, Transiting Planets*. pp 37–43 ([arXiv:0807.1316](#)), [doi:10.1017/S1743921308026215](#)
- Jacklin S., Lund M. B., Pepper J., Stassun K. G., 2015, *AJ*, **150**, 34
- Jacklin S. R., Lund M. B., Pepper J., Stassun K. G., 2017, *AJ*, **153**, 186

- Jacob W. S., 1855, [MNRAS](#), **15**, 228
- Johnson J. A., Winn J. N., Cabrera N. E., Carter J. A., 2009, [ApJL](#), **692**, L100
- Johnson J. A., Winn J. N., Cabrera N. E., Carter J. A., 2010, [ApJL](#), **712**, L122
- Jones M. I., et al., 2018, arXiv e-prints,
- Kendall M., Stuart A., 1977, The advanced theory of statistics. Vol.1: Distribution theory
- Kornilov V., 2012, [MNRAS](#), **425**, 1549
- Law N. M., et al., 2015, [PASP](#), **127**, 234
- Lissauer J. J., 1987, [icarus](#), **69**, 249
- Lithwick Y., Naoz S., 2011, [ApJ](#), **742**, 94
- Lund M. B., Pepper J., Stassun K. G., 2015, *AJ*, **149**, 16
- Mahato S., de Ridder J., Meynants G., Raskin G., van Winckel H., 2018, *IEEE Sensors Journal*, **18**, 2722
- Mann A. W., Gaidos E., Aldering G., 2011, *PASP*, **123**, 1273
- Mayor M., Queloz D., 1995, [nature](#), **378**, 355
- Mayor M., et al., 2003, *The Messenger*, **114**, 20
- McKinney W., 2010, in van der Walt S., Millman J., eds, *Proceedings of the 9th Python in Science Conference*. pp 51 – 56
- Morbidelli A., Brasser R., Tsiganis K., Gomes R., Levison H. F., 2009, [A&A](#), **507**, 1041
- Nielsen L. D., et al., 2019, [A&A](#), **623**, A100
- Oh S., Price-Whelan A. M., Brewer J. M., Hogg D. W., Spergel D. N., Myles J., 2018, [ApJ](#), **854**, 138
- Oliphant T., 2006, *NumPy: A guide to NumPy*, USA: Trelgol Publishing, <http://www.numpy.org/>
- Osborn J., Föhning D., Dhillon V. S., Wilson R. W., 2015, [MNRAS](#), **452**, 1707
- Oswalt T. D., ed. 2003, *The Future of Small Telescopes In The New Millennium. Volume II - The Telescopes We Use Astrophysics and Space Science Library Vol. 288*
- Pepe F. A., et al., 2010, in *Ground-based and Airborne Instrumentation for Astronomy III*. p. 77350F, [doi:10.1117/12.857122](https://doi.org/10.1117/12.857122)
- Pepper J., et al., 2007, [PASP](#), **119**, 923
- Pollacco D. L., et al., 2006, [Publications of the Astronomical Society of the Pacific](#), **118**, 1407
- Price-Whelan A. M., et al., 2018, *AJ*, **156**, 123
- Rappaport S., et al., 2012, [ApJ](#), **752**, 1
- Rappaport S., et al., 2018, [MNRAS](#), **474**, 1453

- Rauer H., et al., 2014, [Experimental Astronomy](#), **38**, 249
- Ricker G. R., et al., 2015, [Journal of Astronomical Telescopes, Instruments, and Systems](#), **1**, 014003
- Rodriguez J. E., et al., 2019, Accepted for publication in AJ, p. [arXiv:1901.09950](#)
- Rosenblatt F., 1971, [icarus](#), **14**, 71
- Rucinski S., Carroll K., Kuschnig R., Matthews J., Stibrany P., 2003, [Advances in Space Research](#), **31**, 371
- Savini et al., 2018. p. 19, [doi:10.1117/12.2233691](#), <https://doi.org/10.1117/12.2233691>
- Schneider, J. Dedieu, C. Le Sidaner, P. Savalle, R. Zolotukhin, I. 2011, [A&A](#), **532**, A79
- Seager S., 2010, Exoplanets
- Southworth J., et al., 2009a, [MNRAS](#), **399**, 287
- Southworth J., et al., 2009b, [MNRAS](#), **399**, 287
- Stefansson G., et al., 2017, [ApJ](#), **848**, 9
- Street R. A., et al., 2003, in Deming D., Seager S., eds, Astronomical Society of the Pacific Conference Series Vol. 294, Scientific Frontiers in Research on Extrasolar Planets. pp 405–408 ([arXiv:astro-ph/0208233](#))
- Struve O., 1952, The Observatory, **72**, 199
- Sullivan P. W., et al., 2015, [ApJ](#), **809**, 77
- Sullivan P. W., et al., 2017, [ApJ](#), **837**, 99
- Swain M. R., Vasisht G., Tinetti G., 2008, [nature](#), **452**, 329
- Takeda G., Rasio F. A., 2005, [ApJ](#), **627**, 1001
- Teachey A., Kipping D. M., 2018, [Science Advances](#), **4**, eaav1784
- Tregloan-Reed J., Southworth J., 2013, [MNRAS](#), **431**, 966
- Trifonov T., Rybizki J., Kürster M., 2019, [A&A](#), **622**, L7
- Udry S., Santos N. C., 2007, [Annual Review of Astronomy and Astrophysics](#), **45**, 397
- Vanderburg A., Johnson J. A., 2014, [PASP](#), **126**, 948
- Vanderburg A., et al., 2016, [ApJL](#), **827**, L10
- Wang S., et al., 2019, [AJ](#), **157**, 51
- Winn J. N., et al., 2007a, [AJ](#), **133**, 1828
- Winn J. N., et al., 2007b, [AJ](#), **134**, 1707
- Wittenmyer R. A., Endl M., Cochran W. D., Hatzes A. P., Walker G. A. H., Yang S. L. S., Paulson D. B., 2006, [AJ](#), **132**, 177

Young A. T., 1967, [AJ](#), 72, 747

Zhao M., et al., 2014, [ApJ](#), 796, 115